Shoc2 Deficiency Disrupts Lymphangiogenesis through mTOR-Mediated Mitochondrial Dysfunction

Patricia Wilson[1], Vishakha Vishwakarma[2], Rebecca Norcross[3], Kashmira Khaire[4], Van N. Pham[2], Brant M. Weinstein[2*], Hyun Min Jung[5*], and Emilia Galperin[1*]

Affiliations

[1] Department of Molecular and Cellular Biochemistry, University of Kentucky, Lexington, KY 40536
[2] Division of Developmental Biology, Eunice Kennedy Shriver National Institute of Child Health and Human Development, NIH, Bethesda, MD 20814, USA.
[3] Clinical Operations R&D group, Zoetis, Kalamazoo, MI, 49001
[4] Department of Molecular and Cellular Developmental Biology, University of California, Los Angeles, CA, 90095
[5] Department of Pharmacology and Regenerative Medicine, University of Illinois at Chicago, Chicago, IL, 60612

*To whom correspondence should be addressed:

Emilia Galperin, University of Kentucky, Department of Molecular and Cellular Biochemistry, 741 S. Limestone St., Lexington, KY 40536. Phone 859-323-1796. Email: emilia.galperin@uky.edu

Hyun Min Jung, Department of Pharmacology and Regenerative Medicine, University of Illinois at Chicago, Chicago, IL, 60612. Email: hmjung@uic.edu

Brant M. Weinstein, Division of Developmental Biology, Eunice Kennedy Shriver National Institute of Child Health and Human Development, NIH, Building 6B, Room 4B4136, Center Drive, Bethesda, MD 20892, Email: weinsteb@nih.gov

Keywords: Shoc2, ERK1/2, Noonan-like syndrome with loose anagen hair (NSLH), IFN, JAK/STAT, mTOR, lymphangiogenesis

ABSTRACT

Shoc2 is a scaffold protein critical for regulating Raf-1 kinase activation and the amplitude of ERK1/2 signals. Hereditary Shoc2 mutations result in Noonan Syndrome with Loose anagen Hair (NSLH), a debilitating congenital disorder associated with lymphatic abnormalities. We demonstrate that zebrafish Shoc2 *null* larvae exhibit nearly a complete loss of lymphatic vasculature, suggesting that the Shoc2 gene plays a critical positive role during developmental lymphangiogenesis. The loss of lymphatics caused by Shoc2 deficiency can be rescued by endothelial autonomous expression of Shoc2, confirming its *in vivo* functional requirement in lymphatic endothelial cells. Shoc2 loss in primary human lymphatic endothelial cells promotes Raptor-mTOR binding and enhances mTORC1 signaling activity. Increased mTORC1 signaling leads to impaired mitochondrial respiration, IRF/IFN-induced signaling, and cell senescence. Notably, expression of the NSLH Shoc2 mutant S2G phenocopies Shoc2 loss, resulting in mTOR activation and increased IFN response. Together, these studies demonstrate the critical role of Shoc2 in lymphangiogenesis and establish a mechanistic link between Shoc2 signaling, mitochondrial function, and lymphangiogenesis, with potential implications for Ras-pathway-related congenital disorders.

INTRODUCTION

The lymphatic vasculature plays a multifaceted role that extends beyond the continuous collection of excess interstitial fluid and macromolecules and the transport of this fluid to the bloodstream. [1] A critical component of the immune system, the lymphatic system serves as a conduit for the trafficking of immune cells and is essential for both adaptive and innate immune responses. [2-4] The intricate function of the lymphatic system, including its role in immune surveillance and response, relies heavily on the precise regulation of lymphatic endothelial cells (LECs). LECs typically reside in a quiescent state, characterized by minimal proliferative activity. This quiescent state, however, is a dynamic equilibrium actively maintained by a complex interplay of intracellular signaling pathways. Disrupting this delicate balance within LECs can have profound consequences. [4,5] Aberrant activation of key signaling cascades, including the PI3K/AKT and Ras/ERK pathways, can drive LECs out of their quiescent state, inducing uncontrolled proliferation and lymphatic malformations that manifest as abnormal lymphatic vessel growth, localized swelling, or more severe conditions, which can significantly impact organ function. [6,7]

The Ras/ERK signaling pathway controls key processes such as cell proliferation, survival, migration, as well as the sprouting of LECs and lymphatic valve development. [7-9] The pivotal role of this pathway in regulating LECs is underscored by syndromes collectively known as RASopathies. [10,11] These spectrum disorders arise from mutations in the genes of the Ras/ERK pathway. More than 20% of RASopathy patients exhibit lymphatic dysfunction presenting in a variety of forms, including lymphedema, a chronic condition characterized by the accumulation of fluid in the interstitial spaces, and more severe conditions, such as chylothorax (fluid in the pleural cavity), hydropericardium (fluid around the heart), or chylous ascites (fluid in the abdomen). [12-14] While lymphatic abnormalities in RASopathies have significant clinical implications, their causes are not fully understood, and it remains unclear why some lymphatic abnormalities may appear later in life and what triggers them.

Noonan Syndrome with loose anagen hair (NSLH) (OMIM #607721) is a RASopathy caused by hereditary variants in the *Shoc2* gene. [15-17] NSLH patients manifest many typical RASopathy presentations, including lymphatic abnormalities. [17-21] Due to the rarity of NSLH, the literature describing the lymphatic presentation is limited, but several studies have reported that patients harboring the Shoc2 variant c. A4>G, p. S2G present with severe lymphatic dysfunction, including fetal hydrops, pleural effusions, and generalized edema resulting in death. [22-24]

Shoc2 is a non-redundant, evolutionarily conserved signaling scaffold protein and a key regulator of Ras/ERK1/2 pathway signal amplitude. [25] Shoc2 tethers Ras and the catalytic subunit of protein phosphatase 1c (PP1c, also known as PP1CA) to dephosphorylate inhibitory phospho-S259 of RAF-1 and accelerate ERK1/2 signals. [26] Shoc2 other interacting partners include the proteins of the ubiquitin system HUWE1, VCP, USP7, PSMC5, and FBXW7 [27-32], scaffold proteins SCRIB and Raptor, and signaling enzymes such as the p110α subunit of phosphatidylinositol 3-kinase (PI3K). [33,34] While the role of these interactions in distinct physiological processes or pathological conditions is unclear, Shoc2's significance in embryonic development, morphogenesis, and the maintenance of various tissues in adult organisms is highlighted in vertebrate models. [35-37] Shoc2 *null* mice and zebrafish CRISPR/Cas9 knockouts both develop systemic deficiencies resulting in early embryonic lethality. [38] Interestingly, zebrafish CRISPR/Cas9 Shoc2 mutants develop unusual edemic swellings, while endothelial-specific Shoc2 knockout in mice causes sporadic hemorrhaging, subcutaneous edema, and fetal lung congestion, suggesting potential vascular deficits in these mutants. [36,38]

Here, we demonstrate that Shoc2 is vital for developmental lymphangiogenesis. Analysis of Shoc2 *null* zebrafish embryos shows a near-total lack of lymphatic vessels. The lack of lymphatic vessels can be rescued by endothelial-specific expression of wild-type Shoc2, demonstrating the endothelial cell-autonomous requirement of Shoc2 for lymphatic development. We also show that Shoc2 loss in primary human LECs impairs mTOR pathway activation, thereby disrupting mitochondrial function, activating nucleic acid sensing machinery, and the IFN/JAK1/STAT1-mediated innate immune response, ultimately leading to cell senescence. Re-expression of wild-type but not NSLH mutant Shoc2 in Shoc2-deficient LECs restores mitochondrial function and reverses innate immune responses. Taken together, this study uncovers the cell-type-specific and essential role of Shoc2 in orchestrating lymphangiogenesis and homeostasis of LECs and provides novel insights into the detailed molecular mechanisms potentially underpinning lymphatic dysfunction in NSLH.

RESULTS

Developmental abnormalities in Shoc2 mutant fish

To understand the role of Shoc2-mediated signaling during lymphatic development, we utilized a stable zebrafish line carrying a germline mutation in the *shoc2* gene. This line, ZDB-ALT-131217-17590, also known as sa24200 (obtained from ZIRC), carries a c.1546G>A mutation that disrupts normal splicing by inserting a 31-bp cryptic exon into the *Shoc2* mRNA (from here, the mutant allele is referred to as $shoc2^{SA}$). The c.1546G>A mutation results in a premature stop codon (p. Val345*) after exon 5 (**Figure S1A-C**). We confirmed this aberrant splicing by sequencing cDNA isolated from 6 days post-fertilization (dpf) $shoc2^{SA/SA}$ larvae. Quantitative PCR revealed a significant reduction in *Shoc2* mRNA levels in $shoc2^{SA/SA}$ larvae compared to controls (**Figure S1D**), and immunoblotting confirmed the absence of Shoc2 protein in $shoc2^{SA/SA}$ larvae (**Figure S1E**). Heterozygous $shoc2^{+/SA}$ alleles did not show a decrease in Shoc2 protein levels. These results indicate that $shoc2^{SA/SA}$ is a loss-of-function mutation that causes nonsense-mediated *Shoc2* mRNA decay. $shoc2^{SA/SA}$ mutants were outcrossed to wild-type fish for at least three generations before further study.

Heterozygous $shoc2^{+/SA}$ carriers were viable and fertile with no apparent abnormalities. However, homozygous $shoc2^{SA/SA}$ larvae displayed severe developmental defects. At 5 dpf, nearly 80% of $shoc2^{SA/SA}$ larvae exhibited edema throughout the whole body, most notably in the heart cavity, trunk, yolk sac, yolk extension, and around the eyes. They also had underinflated swim bladders and were lethargic. These phenotypes closely resemble those observed in our previously described $shoc2^{\Delta 22}$ mutant line (**Figure 1A, B,** and **Figure S1F**). [36] A complementation test using two mutant alleles, $shoc2^{\Delta 22}$ and $shoc2^{SA/SA}$, revealed that a severe edema phenotype can only be found in the $shoc2^{\Delta 22/SA}$ larvae, confirming that the loss of Shoc2 specifically drives the edema phenotype. Survival studies showed that $shoc2^{SA/SA}$ larvae began to die at 6 dpf, with none surviving past 11 dpf (**Figure S1G**). These data demonstrate that the c.1546G>A substitution in *shoc2* severely impairs zebrafish embryonic development.

Morphological analysis of $shoc2^{SA/SA}$ mutants revealed craniofacial abnormalities, including a prominent defect in Meckel's cartilage (curved downwards and shorter than in wild-type larvae) and hypoplastic closure of Meckel's cartilage. Chondrocyte stacking within the cartilaginous elements of $shoc2^{SA/SA}$ was also disorganized (**Figure S2A**). Alizarin Red S staining showed significantly reduced calcification of craniofacial bones in $shoc2^{SA/SA}$ compared to wild-type controls (**Figure S2B**). $shoc2^{SA/SA}$

mutants also displayed abnormal pigmentation, including a loss of iridophores (**Figure S2C, D**) and irregular melanocyte patterning (**Figure S2E**). Collectively, these data demonstrate that the *shoc2* c.1546G>A variant phenocopies the *shoc2*$^{\Delta 22}$ mutant [36], making it a suitable model for further investigation of Shoc2's role in zebrafish development.

Defective lymphatic development in Shoc2 mutant fish

Zebrafish are widely used as a vertebrate model for studying lymphatic development due to their optical clarity, external development, high conservation of the lymphatic vascular system, and the availability of transgenic lines expressing fluorescent reporters in LECs that enable *in vivo* monitoring of lymphatic development. [39,40]. To investigate the role of Shoc2 in lymphatic development and its relation to the edematous phenotype, we crossed the *shoc2*$^{SA/SA}$ mutants with *Tg(mrc1a:eGFP)*^{y251}*;Tg(kdrl:mCherry)*^{y171} double transgenic zebrafish. This line marks lymphatics, arteries, and veins with green, red, or both fluorescent proteins, respectively. [40] We focused on two major lymphatic vascular beds, the trunk and craniofacial lymphatic networks (**Figure 1C**).

At 5 dpf, wild-type larvae exhibited normal lymphatic development, including the thoracic duct (TD), intersegmental lymphatic vessels (ISLV), and dorsal longitudinal lymphatic vessels (DLLV) (**Figure 1D-F**). In contrast, *shoc2*$^{SA/SA}$ mutants showed a marked loss of lymphatic vessels, including the TD, ISLV, and DLLV (**Figure 1G, H**), while blood vessel development remained largely unaffected, indicating that the defects are specific to the lymphatic endothelial cells (**Figure 1I**). Quantification of TD, ISLV, and DLLV formation in wild-type siblings and *shoc2*$^{SA/SA}$ mutants revealed a nearly complete loss of all three sets of trunk lymphatic vessels in Shoc2-deficient animals (**Figure 1J-L**). Craniofacial lymphatic vessels were also strongly reduced in the mutants (**Figure 1M, N**). These findings indicate that lymphatic development is disrupted in Shoc2-deficient zebrafish.

Loss of lymphatic progenitors in Shoc2 mutant fish

Lymphatic network formation in the zebrafish trunk begins with secondary sprouts that emerge from the posterior cardinal vein around 1.5 dpf. [41,42] By 3 dpf, these sprouts contribute to the formation of the parachordal line (PL, or parachordal angioblasts), a transient progenitor structure that gives rise to the trunk lymphatic vessels (**Figure 2A**). Using time-lapse imaging of *Tg(mrc1a:eGFP)*^{y251}*;Tg(kdrl:mCherry)*^{y171} transgenic fish, we analyzed the appearance of secondary sprouts from 32 hours post-fertilization (hpf) to 50 hpf in wild-type siblings (**Figure 2B-D**) and Shoc2

mutants (**Figure 2E-G**). In wild-type siblings, secondary sprouts emerged from the posterior cardinal vein and migrated along the intersegmental blood vessels (**Figure 2B-D** and **Video S1**). In contrast, *shoc2*$^{SA/SA}$ mutants produced only small abortive secondary sprouts up to 50 hpf (**Figure 9E-G** and **Video S2**). By 3 dpf, wild-type siblings formed PLs in the horizontal myoseptum region (**Figure 9H, I**), while *shoc2*$^{SA/SA}$ mutants failed to form PLs (**Figure 2J, K,** asterisks). Quantification of PLs confirmed a near-total loss of PL lymphatic progenitors in *shoc2*$^{SA/SA}$ mutants compared to wild-type siblings (**Figure 2L**).

We also examined the development of the dorsal aorta-derived primary sprouts that generate intersegmental blood vessels by performing time-lapse imaging of *Tg(fli1:eGFP)*^{y1} transgenic zebrafish from 24 to 36 hpf in both wild-type siblings and *shoc2*$^{SA/SA}$ mutants (**Video S3, 4**). Primary sprouts formed normally in both genotypes, suggesting that Shoc2 loss-of-function primarily affects secondary sprout formation but not primary sprouts (**Figure S3)**. These findings indicate that the lymphatic defects in *shoc2*$^{SA/SA}$ mutants are due to the lack of secondary sprout formation and the subsequent failure to produce lymphatic progenitor cells during early larval development.

Endothelial expression of wild-type Shoc2 rescues lymphatic development in Shoc2 mutants.

To examine whether endothelial Shoc2 function is sufficient to support lymphatic development, we drove mosaic transgenic expression of wild-type Shoc2, specifically in venous and lymphatic endothelial cells. We generated *Tol2(uas:mcherry-2A-shoc2)* and control *Tol2(uas:mcherry)* transgenes and injected them separately into single-cell *Tg(mrc1a:KalTA4; UAS:eGFP)* transgenic animals together with a morpholino targeting the translation start site of endogenous but not transgene-driven Shoc2. The animals were raised and examined for PL formation at 3 dpf. As previously reported, morpholino injection phenocopied Shoc2 mutants, resulting in a dramatic loss of PL formation compared to uninjected siblings (**Figure 2M, N, and Q**). Co-injection of the control *Tol2(uas:mcherry)* transgene did not mitigate the effects of the morpholino on lymphatic development, whereas co-injection of the Shoc2-expressing *Tol2(uas:mcherry-2A-shoc2)* transgene strongly rescued parachordal line formation in Shoc2 morphants (**Figure 2P**). These results show that Shoc2 function is required autonomously within endothelial cells to permit lymphatic development to proceed.

Shoc2 controls the amplitude of VEGF-mediated ERK1/2 signals

Recognizing the challenge posed by the near-complete loss of lymphatic vessels in zebrafish Shoc2 *null* larvae for studying LEC homeostasis, we employed human primary lymphatic endothelial cells (HDLEC) as a tractable *in vitro* system to investigate Shoc2 function in these cells. First, we determined that Shoc2 regulates VEGF-initiated activation of the ERK1/2 pathway in HDLEC and human umbilical vein endothelial cells (HUVEC). Shoc2 shRNA depletion (KD) significantly decreased ERK1/2 phosphorylation following stimulation with VEGF-C (HDLEC) or VEGF-A (HUVEC) in both cell types. Conversely, ectopic expression of Shoc2 tagged with tagRFP (SE) rescued ERK1/2 phosphorylation, indicating that Shoc2 is important for VEGF-mediated ERK1/2 signaling in endothelial cells (**Figures 3A-D**). Interestingly, we observed notable changes in the morphology of Shoc2-depleted HDLEC cultured for more than 6 days. To characterize this phenotype, we examined senescence-associated β-galactosidase (SA-β-gal) activity. As shown in **Figure 3E,** almost the entire population of Shoc2-depleted HDLEC was positive for SA-β-gal. Moreover, cell size distribution analysis indicated that Shoc2-depleted cells have larger cell volumes (**Figure 3F**). Shoc2-depleted HDLEC also had increased levels of p53 and phospho-p53, as well as increased levels of senescence-associated cell cycle arrest markers $p21^{Cip1}$ [43] (**Figure 3G**). Together, these data indicate a senescence phenotype in Shoc2-depleted HDLEC. Yet, Shoc2 loss had a minimal impact on HUVEC (**Figure 3G**), suggesting a stringent requirement of Shoc2 for HDLEC proliferation and growth, and implying that the downstream targets of Shoc2-mediated signals potentially involve distinct effector proteins or signaling pathways in the two endothelial cell types.

Transcription changes in Shoc2-depleted HDLEC

To explore the underlying mechanisms of Shoc2 depletion-induced cellular senescence, we performed RNA sequencing of HDLECs expressing nontargeting siRNA (NT, control), cells depleted of Shoc2 using shRNA (KD), or cells expressing both Shoc2 shRNA and siRNA-insensitive Shoc2-tagRFP (SE, rescue) (**Figure 4**). Three days post-transfection, when Shoc2 levels were significantly reduced (validated by western blot, **Figure S4A**), mRNA was isolated from each group for transcriptome profiling. Thorough DESeq2 analysis identified 316 differentially expressed genes (DEGs, fold change ≥ 0.5) across pairwise comparisons of Shoc2 KD and SE cells (Venn diagram, **Figure S4B**). We focused on genes differentially expressed between control (NT) and Shoc2-depleted (KD) cells.

Gene Set Enrichment Analysis (GSEA) using the "Hallmark" database uncovered negative enrichment of gene sets associated with "Cholesterol Homeostasis," "Fatty acid metabolism,"

"Peroxisome," and "MYC targets" (normalized enrichment scores (NES) of -2.28, -1.93, -1.87, and -1.80 respectively). Intriguingly, we observed significant upregulation of "Interferon-alpha response" and "Interferon-gamma response" genes in Shoc2-depleted cells (normalized enrichment scores (NES) of 2.72 and 3.10, respectively) (**Fig. 4A, B,** and **Figure S4C**). Furthermore, we found significant enrichment of gene sets related to "Negative regulation of viral processes," "Antigen processing and presentation," and "Defense response to virus" (normalized p-value = 0.00) using the "Biological Processes" database analysis (**Figure S5A** and **B**). Detailed analysis confirmed increased expression of key genes within the IFN response pathways (**Fig. 4A, B, Figure S5C, D**), including members of the Interferon-Induced Protein with Tetratricopeptide Repeats (IFIT) gene family (e.g., *IFIT1*, *IFIT3*, *IFI27*, *IFI6*, *IFIT30*, *IFIT35*), Interferon-Stimulated Genes (ISGs) such as *ISG15* and *ISG20*, and genes regulating ISGylation (e.g., *USP18* and *HERC6*). [44,45] Many of these upregulated genes contain interferon-sensitive response element (ISRE) *cis*-regulatory sites (e.g., *IFIT3*, *MX1*, *ISG15*) or both ISREs and gamma-activated sequences (GAS) (e.g., *BST2*, *IRF7*, and *OAS1*). [46-48]

qRT-PCR analysis of mRNA isolated from Shoc2-depleted HDLEC 3 and 6 days after transfection corroborated the RNA-seq data (**Figure 4C**) and demonstrated that Shoc2 loss also impacted the expression of lymphatic vascular markers *PROX1* and *LYVE1* (**Figure S6A**). Furthermore, the changes in expression of examined genes were significantly more pronounced at 6 days post-transfection, suggesting an accumulating IFN response upon Shoc2 depletion. Immunoblot analysis confirmed increased expression of IFN response proteins in Shoc2-depleted HDLECs (**Figure 4D**). Shoc2-tagRFP expression rescued the IFN response, confirming the specificity of the Shoc2-depletion-induced gene expression changes. In Shoc2-depleted HDLEC, we also observed a significant increase in the protein levels of IRF7 and IRF9, transcription factors that regulate the production of interferons (IFNs), including IFN-γ. [49] These results indicate that Shoc2 loss in HDLECs induces active transcriptional changes associated with innate immune response.

Shoc2 loss in HDLEC leads to activation of the JAK1/STAT1 intracellular signaling pathway.

Type I and II interferons (IFNs) primarily signal through the Janus-Activated Kinase (JAK)-Signal Transducer and Activator of Transcription (STAT) pathway. [50] As illustrated in **Figure 5A**, this pathway involves JAK activation at the plasma membrane (PM), followed by rapid phosphorylation and nuclear translocation of STAT proteins. These phosphorylated STAT dimers then bind to interferon-stimulated response elements (ISREs) or gamma-activated sequences (GAS) on DNA, initiating the

transcription of interferon-stimulated genes (ISGs). Thus, we investigated whether Shoc2 loss in HDLECs activates the JAK1/STAT1 pathway. Shoc2 depletion significantly increased the phosphorylation of JAK1 (Y1034/1035) and STAT1 (Y701), while expressing Shoc2-tagRFP abrogated this phosphorylation (**Figure 5B**). These findings confirm that in Shoc2-depleted HDLECs, the IFN response coincides with JAK1/STAT1 pathway activation.

Earlier studies reported that ERK1/2 may regulate the expression of CCAAT/enhancer-binding protein-β (C/EBP-β), a transcription factor that governs the expression of various ISGs. [51,52] We, therefore, tested whether inhibiting ERK1/2 activation would mimic the IFN response observed in the Shoc2-depleted HDLECs. **Figure 5C** shows that treatment of Shoc2-depleted, Shoc2-tagRFP-expressing, and control HDLECs with the MEK1/2 inhibitor PD98059 reduced overall levels of ERK1/2 phosphorylation but did not affect either STAT1 phosphorylation or the expression of IFN response proteins (i.e., BST2, ISG15, IRF7, and IRF9). Conversely, the JAK1 inhibitor ruxolitinib effectively eliminated the IFN response and activation of the JAK1/STAT1 pathway in Shoc2-depleted HDLEC (**Figure 5D**). Reduced ERK1/2 phosphorylation observed in cells treated with ruxolitinib is likely a downstream effect of JAK1/STAT1 pathway inhibition, as suggested in [53]. These results demonstrate that IFN response and JAK-STAT pathway activation in HDLEC depleted of Shoc2 are independent of ERK1/2 pathway activity.

Next, we investigated whether Shoc2 loss induces a similar IFN/JAK1/STAT1 response in human umbilical vein endothelial cells (HUVECs). We also examined how the common Shoc2 NSLH-causing variant S2G impacts IFN/JAK1/STAT1 response (**Figure 6**). As expected, Shoc2 loss in HDLECs led to elevated levels of ISGs (i.e., ISG15, MX1, BST2, RSAD2), the transcription factors IRF7 and IRF9, as well as IFN-γ and STAT1 phosphorylation. Notably, in HDLEC depleted of Shoc2 and expressing the Shoc2 S2G variant (S2G), the IFN response and activation of the JAK1/STAT1 pathway were comparable to those of the Shoc2-depleted HDLEC (KD) (**Figure 6A**). Conversely, the IFN/JAK1/STAT1 response remained at basal levels in HUVECs regardless of Shoc2 expression levels or its mutation status (**Figure 6B**). Similarly, Shoc2 loss or expression of the Shoc2 S2G variant in primary fibroblasts did not elicit INF response either **(Figure S7).** These data demonstrate that the aberrant activation of the IFN/JAK1/STAT1 pathway observed following Shoc2 depletion or expression of the S2G variant is unique to HDLECs.

Activation of RIG-I-like receptor signaling pathway in Shoc2-depleted HDLEC

Additional transcriptome analysis of Shoc2-depleted HDLEC revealed significant enrichment of genes involved in the RIG-I-like receptor (RLR) signaling pathway (KEGG pathway, NES 1.49). Key RLR pathway genes, including *IFIH1* (MDA5), *DDX60*, *DDX58* (RIG-I), *TRIM25*, and *TRIM14*, were significantly upregulated in Shoc2-depleted cells (**Figure 7A**). MDA5 and RIG-I are cytoplasmic pattern recognition receptors that detect viral double-stranded RNA (dsRNA) and trigger an innate immune response. A crucial step in an innate immune response involves the recruitment of MAVS (mitochondrial antiviral signaling protein) located on the outer membrane of mitochondria. The MDA5-MAVS interaction triggers the activation of key transcription factors, including IRF7 and IRF9, which in turn drive the production of IFN and other pro-inflammatory cytokines (**Figure 7B**). [54] qRT-PCR confirmed the increased expression of *MDA5* (*IFIH1*), *RIG-I* (*DDX58*), and other RLR response components (e.g., E3 ligases *TRIM25* and *TRIM14*, and helicase *DDX60*) in Shoc2-depleted HDLEC. Interestingly, *MDA5* and *RIG-I* expression was significantly elevated as early as 3 days post-transfection (**Figure 7C**).

MDA5 phosphorylation is critical for its activation. [54,55] Specifically, protein phosphatases PP1cα and PP1cλ-mediated dephosphorylation of Ser88 is essential for activating MDA5 and reversing its signaling-repressed state. [55] Moreover, for MDA5 to translocate to mitochondria and initiate an innate immune response, both dephosphorylation of Ser88 and ISGylation are necessary. [56,57] We found that increased MDA5 expression (**Figure 7D, input**) correlated with significantly decreased Ser88 phosphorylation on MDA5 precipitated from either Shoc2-depleted or S2G-expressing HDLECs (**Figure 7D, IP**), indicating the MDA5 activation. Yet, Ser88 phosphorylation of MDA5 or its levels remained unchanged in HUVEC cells regardless of Shoc2 levels (**Figure 7E**).

Next, we used MAVS- or MDA5-specific siRNAs to probe whether MDA5 and MAVS drive the IFN response [57] in Shoc2-depleted HDLECs (**Figure 7F**). We found that MDA5 depletion abrogated the IFN response (as assessed by BST2, RSAD2, MX1, and ISG15 expression) and the JAK1/STAT1 pathway activation (as assessed by JAK1 and STAT1 phosphorylation) in Shoc2-depleted HDLEC. siRNA depletion MAVS also markedly reduced the IFN-JAK1/STAT1 response (**Figure 7F**), demonstrating that IFN-JAK1/STAT1 pathway activation in the Shoc2-depleted HDLEC depends on the MDA5-MAVS cytoplasmic pattern recognition response.

Mitochondrial dysfunction of Shoc2-depleted HDLEC

The outer mitochondrial membrane protein MAVS is involved in maintaining mitochondrial homeostasis and regulating mitochondrial dynamics, including mitochondrial fusion and fission. [58,59] Hence, we investigated the effects of Shoc2 loss on mitochondrial function. Compared to controls, phosphorylation of mitochondrial fission marker Drp1 (Ser616) was significantly increased in Shoc2-depleted HDLECs and cells expressing the Shoc2 S2G variant (**Figure 8A**). While total DRP1 protein levels remained constant, the levels of other proteins involved in mitochondrial fusion dynamics, including MTFP1, MFF, and OPA1, were altered by the Shoc2 loss. Additional transcriptome analysis uncovered changes in the expression of genes involved in oxidative phosphorylation (OXPHOS), including those encoding ATP synthase, cytochrome c oxidase, and other electron carriers (**Figure S8**).

Next, we examined whether mitochondrial respiration was affected by the Shoc2 loss (**Figure 8B**). Seahorse live cell metabolic flux analysis revealed a significant decrease in basal but not maximal consumption rates (OCR) (**Figure 8C, D**). We also found that mitochondrial ATP production (**Figure 8E**) and proton leak (**Figure 8F**) were significantly decreased in cells depleted of Shoc2 or expressing the Shoc2 S2G variant. Together, these data indicate that mitochondrial function is impaired in cells depleted of Shoc2 or expressing the NSLH variant S2G.

Regulation of the mTOR pathway by Shoc2

The findings that the upregulated IFN-JAK1/STAT1 response is independent of Shoc2's role in ERK1/2 pathway activation (**Figure 5**) and that there were impairments in mitochondrial function in Shoc2-depleted HDLECs (**Figure 8**) prompted us to investigate other signaling mechanisms potentially dysregulated in Shoc2-depleted HDLECs. Previous work has shown that Shoc2 negatively regulates mTORC1 signaling by competing with mTOR for binding of Raptor, a key mTORC1 complex component (**Figure 9A**). [28,60] Thus, we examined the effect of Shoc2 loss on mTOR pathway activation in HDLECs (**Figure 9B**). In Shoc2-depleted or S2G variant-expressing HDLECs, increased mTOR phosphorylation correlated with increased phosphorylation of mTOR downstream substrates (i.e., eukaryotic translation initiation factor 4E-binding protein 1 (4E-BP1) and ribosomal protein S6 kinase beta-1 (S6K1)), indicating enhanced mTORC1 activity. Using immunoprecipitation, we showed that Raptor-mTOR binding significantly increased in HDLEC depleted of Shoc2 or expressing the Shoc2 S2G variant. Conversely, the expression Shoc2-tagRFP reduced Raptor interaction with mTOR (**Figure 9C**). Neither the Shoc2 deletion nor the expression affected mTOR-Rictor binding (**Figure 9C, F**). Interestingly, mTOR pathway hyperactivation was not observed in Shoc2-depleted HUVECs (**Figure**

9D). While mTOR immunoprecipitation showed a slight increase in Raptor-mTOR binding in Shoc2-depleted HUVEC and cells expressing the Shoc2 S2G variant, the densitometric ratio of Raptor to mTOR was significantly lower in Shoc2-depleted HUVEC (1:0.2) than observed in HDLECs (1:1), which may account for the lack of mTOR signaling upregulation in Shoc2-depleted HUVECs (**Figure 9E**).

To confirm the mechanistic link between mTORC1 activation and the IFN response in Shoc2-depleted HDLEC, cells were treated with the mTOR inhibitor Rapamycin. Rapamycin treatment effectively blunted mTOR signaling and blocked the IFN/JAK/STAT response in Shoc2-depleted and S2G-expressing HDLECs (**Figure 9F**). These data demonstrate that mTORC1, but not mTORC2, mediates the effect of Shoc2 on IFN signaling in HDLEC and indicate that the Shoc2-Raptor-mTOR equilibrium is critical for maintaining proper levels of mTOR signals in HDLECs. Shoc2 loss or the presence of the S2G mutant disrupts this equilibrium, leading to increased Raptor-mTOR binding. Together, the results presented in **Figures 3-9** suggest that in the absence of Shoc2, hyperactive mTORC1 signaling alters mitochondrial function, which could explain the increased mitochondrial fission, activation of the IFN/JAK/STAT response, and, ultimately, cell senescence (**Figure 9G**).

DISCUSSION

Lymphatic vessel development and homeostasis are complex processes governed by diverse signaling pathways. [1,6,61] Our study reveals a novel and essential role for the signaling scaffold Shoc2 in lymphatic regulation, demonstrating its complex influence on cellular signaling and homeostasis. Specifically, Shoc2 loss ablates lymphatic vasculature *in vivo*, while its deficiency in LEC induces (1) activation of mTOR and IFN/JAK/STAT signaling pathways, (2) altered mitochondrial respiration and function, and (3) cellular senescence. Notably, the Shoc2 (S2G) NSLH variant recapitulates the mitochondrial dysfunction, mTOR activation, and IFN/JAK/STAT pathway dysregulation observed in Shoc2-depleted LECs. Thus, this study establishes a novel mechanistic link between the Shoc2 scaffold, mitochondrial function, mTOR signaling, and innate immune response in lymphatic cells. Importantly, these effects are cell-type specific, as Shoc2 depletion in primary fibroblasts and vein endothelial cells did not elicit mTOR pathway activation or immune responses. The differential cellular responses to the loss of this ubiquitously expressed signaling scaffold warrant further investigation to explore whether cell developmental origin, cellular state (proliferating vs. quiescent), or differences in upstream signaling are factors contributing to these cell-specific outcomes.

The embryonic lethality of conventional Shoc2 knockout mice at E8.5, with partial embryo absorption occurring before the onset of lymphangiogenesis, has limited *in vivo* studies. [38] Thus, the Shoc2 mutant zebrafish is currently the sole vertebrate model for examining global Shoc2 loss *in vivo*. Our previous work has demonstrated severe developmental defects in the neural crest of *shoc2* mutant zebrafish. [36,62] This study highlights the significance of Shoc2 for lymphangiogenesis and demonstrates a Shoc2-autonomous function in lymphatic endothelium (**Figures 1-2**). Shoc2 mutant zebrafish exhibit a striking loss of facial and trunk lymphatic vessels with no apparent effect on other endothelial cells. Given the high homology between zebrafish and human Shoc2, along with ubiquitous expression, these findings are highly relevant to human biology. Our endothelial-specific transgenic Shoc2 "rescue" experiments demonstrate the endothelial-autonomous requirement for lymphatic development and show that the endothelial function of Shoc2 is sufficient for normal lymphatic development. Future studies will investigate whether the tissue microenvironment (e.g., stiffness, immune cell composition) impacts Shoc2 function in different endothelial cells.

Shoc2 function in lymphatic endothelial cells: mechanisms

Beyond showing Shoc2's importance in developmental lymphangiogenesis, this study elucidates the molecular mechanisms by which Shoc2 maintains lymphatic endothelial cell homeostasis. Shoc2

function is best understood within the context of the ERK1/2 pathway and its role in mRas-Shoc2-PP1c holoenzyme. [63] Multiple labs, including ours, have demonstrated that Shoc2 regulates the ERK1/2 phosphorylation amplitude, as well as the proliferation and motility of various immortalized or cancer cell types.[64,65] More recently, Shoc2 has been implicated in regulating mTORC1 signals impacting growth, survival, and tumorigenesis of pancreatic, lung, and liver cancer cells. [28,66] However, with the exception of mouse neural progenitors, Shoc2 function in primary cells remains largely unexplored. We provide compelling evidence that, in primary lymphatic endothelial cells, Shoc2 regulates VEGF-ERK1/2 activity and balances mTORC1 signals (**Figures 3, 5 and 9**). Consistent with mTORC1's well-established role in regulating mitochondrial function (i.e., fission, fusion, etc.) and cellular senescence [67-71], we observed that upregulated mTORC1 in the Shoc2-depleted cells leads to mitochondrial dysfunction. Thus, given mTORC1's pleiotropic roles in cellular processes, such as nutrient/energy sensing, protein synthesis, and metabolism, additional work to fully elucidate the spectrum of Shoc2's effects on cellular homeostasis, particularly its role in adaptive autophagy and nutrient sensing, will be critical.

In this study, we also provide new evidence that Shoc2 dysfunction impacts mitochondria-regulated innate immune response (**Figure 8**). Mitochondria function as both energy providers and signaling hubs in the innate immune response. To regulate immune responses, mitochondria release signals like mitochondrial DNA (mtDNA), RNA (mtRNA), and reactive oxygen species (ROS). [59,72] Our findings of increased expression and activation of MAVS and the pattern recognition receptors, RIG1 and MDA5 (**Figure 7**), suggest that hyperactive mTORC1 induces mitochondrial dysfunction of Shoc2-depleted LECs. While mitochondrial dsRNA is the likely trigger of the response in Shoc2-depleted cells, additional studies are needed to confirm this. Yet, it is reasonable to assume that in the absence of Shoc2, mt-dsRNA activates RIG1/MDA5, triggers MAVS and IRF-7/9 signaling, leading to proinflammatory cytokine and interferon production, and ultimately contributes to cellular stress and senescence (**Figure 9G**). Importantly, our data indicate that Shoc2's role in MDA5 activation is independent of the Shoc2-PP1c-MRas holoenzyme, as PP1c was absent from mTOR-Shoc2 immunoprecipitates and MDA5 Ser338 was dephosphorylated in Shoc2-depleted cells. Whether the exceptional sensitivity of lymphatic endothelium to Shoc2 dysfunction is related to the requirement to limit mTORC1 signals to maintain cell quiescence will also be explored in the following investigations.

The IFNγ inhibitory effects on lymphatic vessels are well-documented. [1,73,74]. IFNγ treatment reduces the expression of the key lymphatic transcription factor PROX-1 and the membrane

glycoprotein LYVE-1 and suppresses lymphatic growth *in vitro*. [73-75] Given the observed increase in IFNγ signaling in Shoc2-depleted cells, it is plausible that IFNγ contributes to their senescence. Moreover, IFNγ's precise influence on lymphangiogenesis may depend on factors such as other cytokines or the specific type of lymphatic endothelial cell involved. Future studies will determine if elevated IFNγ levels in lymphatic progenitor cells underlie the lymphatic vessel defects observed in Shoc2 knockout larvae. Considering the emerging role of lymphatic cells in shaping local immune responses [76], it is essential to investigate whether lymphatic cells in NSLH patients modulate adaptive immunity or antigen presentation. The physiological consequences of the Shoc2 S2G-associated IFN response on lymphatic vessel development and the potential contribution of chronic IFN activation to lymphatic dysfunction also warrant thorough investigation. Such studies will be in line with the recent findings demonstrating Shoc2's involvement in the immune signaling of invertebrate antibacterial and eukaryotic antiviral responses. [77,78]

Implications for NSLH pathology

Our finding that, in lymphatic cells, the Shoc2 NSLH variant S2G fails to compete with mTOR for Raptor binding effectively, and similarly to the Shoc2 loss, disrupts mitochondrial function and triggers IFN response is one of the most interesting observations of this study. The Shoc2 S2G variant localizes to the PM due to aberrantly acquired *N*-myristoylation. [79] Thus, it is tempting to speculate that these Shoc2-Raptor-mTOR complexes are spatially defined. However, the molecular details of why this variant, despite being able to bind mTOR, still causes increased mTOR activity remain to be elucidated. Notably, mitochondrial dysfunction, decreased adipogenesis, fat malabsorption, increased energy expenditure, and enhanced insulin signaling are found in other RASopathies. [80-83] For instance, PTPN11 mutations causing Noonan syndrome reduce mitochondrial membrane potential and ATP content while increasing ROS levels. [84 85,86] Similarly, B-RAF and NF1 mutations affect mitochondrial respiration. While the specific mechanisms and downstream effectors contributing to mitochondrial dysfunction in different RASopathies are still unclear, our findings underscore the need for further research to define the mechanistic link between mitochondrial dysfunction and mutations in specific RASopathy genes.

Intriguingly, RASopathy patients, including those diagnosed with NSLH, exhibit an increased risk of autoimmune disorders. [87-89] Individuals with the Shoc2 S2G variant exhibit autoimmune manifestations such as systemic lupus erythematosus, autoimmune cytopenia, and autoimmune thyroiditis. [87,90-93] Despite this association, the triggers for clinically overt disease remain poorly understood. Therefore, our discovery of a link between mitochondrial dysfunction, IFN response, and

cellular homeostasis in Shoc2-deficient lymphatic cells potentially provides a novel mechanism underlying the autoimmune presentation in NSLH patients.

In conclusion, we have established that the progressive IFN response observed in both Shoc2-deficient cells and cells expressing the NSLH S2G variant depends on upstream mTOR signaling and can be abrogated by treatment with the mTOR inhibitor rapamycin. Our findings underscore the critical role of Shoc2 as a molecular gatekeeper that balances ERK1/2 and mTOR signals, highlighting its cell-type-specific functions. We also provide novel insights into the roles of ERK1/2 and mTOR during developmental lymphangiogenesis, opening new avenues for understanding how these pathways contribute to lymphatic development and related disorders. These results raise critical questions for future research and emphasize the need for a deeper understanding of Shoc2's multifaceted role in healthy and diseased organisms. Therapies combining ERK1/2-targeting therapies with mTOR inhibition may be relevant for treating RASopathies. Given the intricate interplay between Shoc2, IFN response, and mTORC1, targeting these pathways holds significant therapeutic potential for diseases associated with lymphatic dysfunction or aberrant immune activation. Specifically, JAK or mTOR inhibitors may offer therapeutic benefits for patients with Shoc2 mutations, potentially mitigating the observed lymphatic and immune-related pathologies.

MATERIALS AND METHODS

Antibodies and other reagents

Table S1 lists the specific primary and secondary antibodies used for protein detection. Ruxolitinib and PD98059 were purchased from LC Labs, and hexadimethrine bromide (polybrene) was obtained from Sigma-Aldrich.

Constructs

tagRFP-tagged Shoc2 (Shoc2-tRFP), the pLVTHM constructs expressing Shoc2 short hairpin RNA (shRNA), and nontargeting shRNA were described previously. [94,95] The pLVTHM constructs expressing Shoc2 and nontargeting shRNA also express GFP to visualize transfected cells. [95]

Cell culture and lentivirus transduction

Human dermal lymphatic endothelial cells (HDLEC) (PromoCell) and normal human umbilical vein endothelial cells (HUVEC) (Lifeline Cell Technology) were grown in VascuLife basal media (Lifeline Cell Technology) containing 5 ng/mL rh FGF basic, 50 µg/mL ascorbic acid, 1 µg/mL hydrocortisone hemisuccinate, 2% FBS, 10 mM L-glutamine, 15 ng/mL rh IGF-1, 5 ng/mL rh EGF, 5 ng/mL rh VEGF, 0.75 U/mL heparin sulfate, and supplemented with 30 µg/mL gentamicin and 15 ng/mL amphotericin B.

For lentivirus transduction, cells were plated in 12-well dishes at 50–60% confluence. The ratio of viral particles to target cells was determined for each viral prep. The lentiviral stock was diluted in a fresh culture medium containing polybrene. Shoc2–tagRFP (SE or S2G) and shShoc2/GFP (KD), or non-targeting-GFP (NT) fluorescence, were detected 36–48 h after lentivirus transduction. The efficiency of shRNA knockdown and cDNA expression was validated using Shoc2-specific antibodies 3 days after lentivirus transduction.

Real-time quantitative PCR (qPCR)

Total RNA was isolated from cells using a PureZOL/Aurum total RNA isolation kit (Bio-Rad) according to the manufacturer's instructions. Aliquots containing equal amounts of RNA were subjected to reverse transcription-PCR (RT-PCR) analysis. Quantitative RT-PCR was performed using SoAdvanced SYBR Green Supermix and a Bio-Rad CFX detection system (Bio-Rad). Sequence-specific primer sets are listed in **Table S2**. HPRT1 mRNA was used as a reference gene. The relative

amounts of RNAs were calculated using the comparative threshold cycle method. The values for the samples were normalized against those for the reference gene, and the results are presented as the fold change in the amount of mRNA recovered from cells transfected with nontargeting siRNA. The data represent the mean standard deviations (SDs) from two independent experiments.

siRNA transfections

To silence protein expression by RNA interference, cells were seeded in 12-well plates (at 50 to 60% confluence with 1 ml of VascuLife media per well) at least 20 h before transfection. Small interfering (siRNA) transfections were performed according to the manufacturer's recommendations, using Dharmafect reagent 2 (Dharmacon). The siRNA sequences used to target MDA5 and MAVS are listed in **Table S4.** The efficiency of the siRNA knockdown was validated by western blotting.

Immunoprecipitation

Cells were placed on ice and washed with Ca^{2+}, Mg^{2+}-free phosphate buffered saline (PBS), and the proteins were solubilized in 50 mM Tris (pH 7.5) containing 150 mM NaCl, 1% Triton X-100, 1 mM Na_3VO_4, 10 mM NaF, 0.5 mM phenylmethylsulfonyl fluoride (PMSF, Sigma, St. Louis, MO, USA), 10 µg/ml of leupeptin, and 10 µg/ml of aprotinin (Roche, Basel, Switzerland) for 15 min at 4°C. Lysates were centrifuged at 14,000 *rpm* for 15 min to remove insoluble material. Lysates were incubated with appropriate antibodies for 2 hrs, and the immunocomplexes were precipitated using protein A- or G-Sepharose (GE Healthcare Life Sciences, Chicago, IL, USA). Immunoprecipitates and aliquots of cell lysates were denatured in a sample buffer at 95°C, resolved by electrophoresis by SDS-PAGE, transferred to a nitrocellulose membrane, and probed by western blotting with various antibodies, followed by chemiluminescence detection.

mTOR immunoprecipitation was done following the protocol of Kim et al. 2002. Briefly, cells were rinsed once with PBS, lysed in 600 µl of ice-cold lysis buffer (40 mM HEPES [pH 7.5], 120 mM NaCl, 1 mM EDTA, 50 mM NaF, 1.5 mM Na3VO4, 0.5 mM phenylmethylsulfonyl fluoride, 10 µg/ml of leupeptin, and 10 µg/ml of aprotinin and 0.3% CHAPS) and incubated for 30 min on ice. After clearing, 40 µl of a 50% slurry of protein G-Sepharose and 4 µg of the anti-mTOR antibody were added to the supernatant and rotated for 3 hrs at 4 °C.

Western blot analysis

Cells were placed on ice and washed with Ca^{2+}, Mg^{2+}-free phosphate buffered saline (PBS), and the proteins were solubilized in 50 mM Tris (pH 7.5) containing 150 mM NaCl, 1% Triton X-100, 1 mM Na_3VO_4, 10 mM NaF, 0.5 mM phenylmethylsulfonyl fluoride (PMSF, Sigma, St. Louis, MO, USA), 10 μg/ml of leupeptin, and 10 μg/ml of aprotinin (Roche, Basel, Switzerland) for 15 min at 4°C. Lysates were centrifuged at 14,000 *rpm* for 15 min to remove insoluble material. Aliquots of cell lysates were denatured in a loading buffer at 95°C, resolved by electrophoresis, and probed by western blotting with various antibodies, followed by chemiluminescence detection. Proteins transferred from SDS-polyacrylamide gels to nitrocellulose membranes were visualized using a ChemiDoc analysis system (Bio-Rad, Hercules, CA, USA). Several exposures were analyzed to determine the linear range of the chemiluminescence signals. Quantification was performed using the densitometry analysis mode of Image Lab software (Bio-Rad, Hercules, CA, USA). To visualize proteins with close molecular weight, in some instances, several identical SDS-PAGE gels were used to resolve protein lysates.

Seahorse extracellular flux analysis

The Seahorse XF96 Extracellular Flux Analyzer (Agilent) was used to measure cellular respiration activity in HDLEC. Cells were seeded at a density of 2×10^4 cells per well in an XF96 plate ~12 h before the measurement. The following day, cells were washed twice with assay medium (unbuffered DMEM supplemented with 25 mM glucose, 2 mM L-glutamine, and 1 mM pyruvate) and incubated at 37°C in a non-CO2 incubator for 1 hour. OCR was measured at baseline and following sequential injections of oligomycin (1 μM), carbonyl cyanide-4-(trifluoromethoxy)phenylhydrazone (FCCP) (1.5 μM), and rotenone/antimycin A (0.5 μM). Data were normalized to total protein content determined by a BCA assay.

The mitochondrial stress tests were performed per the manufacturer's protocol. The relative levels of non-mitochondrial, basal, maximal, and ATP production-related respiration were calculated using the Mito stress tests using the Seahorse Wave software (Agilent) for XF analyzers.

Cell senescence assay

HDLEC were stained for senescence-associated β-galactosidase activity using the β-Galactosidase Staining Kit (Cell Signaling) according to the manufacturer's recommendation. Briefly, equal numbers of cells 2×10^4 were washed once with 1X PBS and then fixed. Cells were incubated with the β-

Galactosidase Staining Solution ON at 37°C for at least overnight. Cells were overlaid with 70% glycerol for long-term storage and stored at 4°C. To quantify cells stained for senescence-associated β-galactosidase activity, we acquired GFP fluorescence to visualize the transfected cells. The percentage of senescent cells was divided by the total number of cells counted using immunofluorescence (n = 3 dishes per genotype).

Zebrafish strains and maintenance

This study was conducted in AAALAC-accredited facilities under active research projects approved by the University of Kentucky Animal Care and Use Committee (#2019-3208), the University of Illinois at Chicago Animal Care and Use Committee (#23-112), and the *Eunice Kennedy Shriver* National Institute of Child Health and Human Development (Animal Study Proposal #21-015, 24-015). All zebrafish strains were bred, raised, and maintained according to established animal care protocols for zebrafish husbandry. Embryos were staged as previously described. [96] The following transgenic and mutant zebrafish lines were used in this study: *Tg(mrc1a:eGFP)*^{y251} [40], *Tg(kdrl:mcherry)*^{y205} [97], and *Tg(fli1:eGFP)*^{y1}.[98] The *Tg(mrc1a:KalTA4)* line was generated from this study. The *Tg(UAS:eGFP)* line was generously provided by the Kawakami lab. The *shoc2*$^{\Delta 22}$ has been previously described in [36], and the *shoc2*$^{SA/SA}$ line was obtained from the Sanger Institute Zebrafish Mutation Project.

Generation of transgenic zebrafish lines

The *mrc1a:KalTA4* transgene construct was assembled using an LR recombination reaction, using the destination vector *pDestTol2pA/pA2* [99] and three entry clones: *p5E-mrc1a* [40], *pME-KalTA4* (PCR-amplified from plasmid #10080, Addgene), and *p3E-polyA* from the Tol2kit.[99] The pME-KalTA4 construct was amplified using primers containing attB1/attB2 sites, and then cloned into the pDONR211 vector using BP Clonase (Cat# 11789-020, Thermo Fisher Scientific). The transgenic line *Tg(mrc1a:KalTA4)* was generated by microinjecting the *mrc1a:KalTA4* transgene construct (55 pg) along with *Tol2* transposase (50 pg) into one-cell stage zebrafish embryos from the *Tg(UAS:eGFP)* line. Embryos were subsequently screened for GFP expression in the lymphatic vasculature, leading to the establishment of the germline-transmitting line *Tg(mrc1a:KalTA4;UAS:eGFP)* ^{y721}.

Imaging methods

Embryos were anesthetized using 1x tricaine, mounted in 0.8-1.5% low-melting-point agarose dissolved in egg water, and mounted on a depression slide. [100] Confocal images were acquired using a Nikon Ti2 inverted microscope with a Yokogawa CSU-W1 spinning disk or a Zeiss LSM880 microscope. Brightfield images were obtained using a Leica M205 microscope. The images were analyzed using ImageJ, Adobe Photoshop (Adobe), and NIS-Elements (Nikon) software.

Morpholino injection

All MOs were obtained from Gene Tools, LLC (Philomath, OR) and injected into 1-2 cell stage zebrafish embryos. The following MOs were used in this study: standard control MO: 5'-CCTCTTACCTCAGTTACAATTTATA-3'; *shoc2* MO1: 5'-TACTGCTCATGGCGAAAGCCCCGCA-3'. Embryos were injected with 5.2 ng of Shoc2 MOs.

Shoc2 expression construct

The 6x-UAS:mCherry-2A-shoc2 construct was generated through a three-part LR recombination reaction using Gateway Technology. This process involved the creation of three entry clones and a destination vector. The 5' entry clone (p5E 6xUAS) was constructed via traditional cloning methods. A linearized p5E-MCS vector, digested with XhoI and SpeI, served as the backbone, into which a 6xUAS fragment was inserted. This fragment was PCR-amplified from the 6x-UAS:EGFP plasmid, kindly provided by Marnie Halpern. The middle entry clone (pME mCherry-2A-shoc2) was generated using SLiCE (Seamless Ligation Cloning Extract, where 3 fragments were assembled by short stretches of homologous DNA recombination with the PPY SLiCE strain. The first fragment was a linearized pME-MCS vector, digested with EcoRI and SpeI. The second fragment was a PCR-amplified mCherry-2A fragment from a plasmid encoding mCherry-2A, and the third fragment was a full coding sequence of zebrafish shoc2 amplified using PCR. The 3' entry clone, p3E polyA, containing the polyA sequence, was obtained from the Tol2kit. [99] The final 6xUAS mCherry-2A-shoc2 construct was assembled by performing an LR recombination reaction using the destination vector, pDestTol2pA/pA2 [99], resulting in the insertion of the three entry clones into the destination vector.

Shoc2 rescue in zebrafish

Shoc2 rescue experiments were conducted in shoc2 morphants with the *Tg(mrc1a:kalTA4; UAS:eGFP)* transgenic background for endothelial rescue. The shoc2 MO (5'-

TACTGCTCATGGCGAAAGCCCCGCA-3'; Gene Tools, LLC) was used at a concentration of 4.6 ng per embryo. For Shoc2 expression rescue, embryos were injected with either 6x-UAS:mCherry-2A-shoc2 or 6x-UAS:mCherry (control group) at a concentration of 40-45 ng per embryo, with or without shoc2 MO. DNA constructs were injected at the one-cell stage, followed by MO injection into the yolk at the one-to-four-cell stage. Image acquisition was performed using a Nikon Ti2 inverted microscope with Yokogawa CSUW1 spinning disk confocal, with the 10× Air 0.45 NA objective.

Analysis of RNA-seq data

mRNAs were isolated from HDLECs expressing Shoc2 shRNA. For library preparation, mRNA was first extracted from total RNA using oligo (dT) magnetic beads and sheared into short fragments of about 200 bases. The cDNA library was sequenced using the Illumina NextSeq 500 sequencer. Quality control (QC) of the raw sequence data was performed using FastQC (version 0.11.7). The concatenated sequences were directly aligned to the Homo Sapience GRCh38 reference genome assembly (GRCh38) using STAR (version 2.6), generating alignment files in bam format. Sequencing reads were trimmed and filtered using Trimmomatic (V0.39) [101] to remove adapters and low-quality bases. Trimmed reads were mapped to the human reference genome assembly GRCh38 transcripts annotation using RSEM. [102] RSEM results normalization and differential expression analysis were performed using the R package EdgeR. [103] Significantly up-/downregulated genes between groups were determined as fold change >= 2 and q-value <0.05. Transcript per million were used for generating heatmaps, with represented values ranging from +1.5 (red, high expression) to −1.5 (blue, low expression). The RNA-seq data is publicly available as GEO series GSE288882. The data is MIAME compliant (https://www.ncbi.nlm.nih.gov/geo/query/acc.cgi?acc=GSE288882).

The gene set enrichment analysis was performed using GSEA software and the gene sets in the Molecular Signature Database (MSigDB). [104] As recommended for GSEA from RNA sequencing experiments, genes with no counts in any sample were removed, along with low-expressing genes (mean or geometric mean <10 reads across all samples). As recommended in the GSEA user guide (https://www.gsea-msigdb.org/gsea/doc/GSEAUserGuideFrame.html), a false discovery rate (FDR) cut of 25% was used for Hallmark, KEGG, and Biological pathway gene set analysis. These data were the basis for the Venn diagram, heatmaps, and KEGG pathway analysis.

Statistical analyses

Results are expressed as means ± S.D. The statistical significance of the differences between groups was determined using a *t*-test or one-way and two-way ANOVA (followed by Dunnett's test). p 0.01 to 0.05 was considered statistically significant. (*p = 0.01 to 0.05, **p = 0.001 to 0.01, ***p = 0.0001 to 0.001, ****$p < 0.0001$, ≥ 0.05- non-significant, ns). GraphPad Prism 8.0 (GraphPad Prism Software Inc., Chicago, IL, USA) was used to perform all statistical analyses.

Data availability

This published article and its supporting information files include all data generated or analyzed during this study.

Supporting information **-** This article contains supporting information.

Acknowledgments

We thank Dr. Tianyan Gao for critically reading the manuscript and for valuable reagents, and Dr. Saurabh Chattopadhyay and Dr. Michaela Guck for valuable reagents. We also thank Ms. Lina Abdelmoti for the excellent care of the zebrafish colony.

Funding

This project was supported by grants from the National Institute of General Medical Sciences (R35GM136295 and 1S10OD025033-01 to EG). BMW was supported by the intramural program of the *Eunice Kennedy Shriver* National Institute of Child Health and Human Development (ZIA-HD001011 and ZIA-HD008808). This research was supported by the Biostatistics and Bioinformatics and Redox Metabolism Shared Resources of the University of Kentucky Markey Cancer Center (P30CA177558). Its contents are solely the authors' responsibility and do not necessarily represent the official views of the National Institute of Health. HMJ was supported by the UIC College of Medicine start-up fund.

Conflict of interest statement: none declared.

FIGURE LEGENDS

Figure 1. Loss of lymphatics in shoc2 mutant zebrafish.

A. Brightfield images of a lateral view of the entire zebrafish larvae of wild-type sibling (top panel) and *shoc2*$^{SA/SA}$ mutant (bottom panel). The red arrow is pointing to an edematous site.

B. Brightfield images of a dorsal view of the entire zebrafish larvae of wild-type sibling (top panel) and *shoc2*$^{SA/SA}$ mutant (bottom panel). Red arrows are pointing to edematous sites.

C. Schematic of areas of confocal imaging highlighting the trunk and craniofacial vessels.

D. Confocal image of trunk vessels of wild-type sibling *Tg(mrc1a:eGFP)*^{y251}*;Tg(kdrl:mCherry)*^{y171} zebrafish larvae at 5 dpf. Scale bar: 100 µm. TD, thoracic duct; ISLV, intersegmental lymphatic vessel; DLLV, dorsal longitudinal lymphatic vessel.

E. Confocal image of trunk vessels of a wild-type sibling *Tg(mrc1a:eGFP)*^{y251} showing a separated green channel from panel D. Scale bar: 100 µm.

F. Confocal image of trunk vessels of a wild-type sibling *Tg(kdrl:mCherry)*^{y171} showing a separated red channel from panel D. Scale bar: 100 µm.

G. Confocal image of trunk vessels of a *shoc2*$^{SA/SA}$ mutant *Tg(mrc1a:eGFP)*^{y251}*;Tg(kdrl:mCherry)*^{y171} zebrafish larvae at 5 dpf. Asterisks indicate the absence of lymphatic vessels. Scale bar: 100 µm.

H. Confocal image of trunk vessels of a *shoc2*$^{SA/SA}$ mutant *Tg(mrc1a:eGFP)*^{y251} showing separated green channel from panel D. Scale bar: 100 µm.

I. Confocal image of trunk vessels of a *shoc2*$^{SA/SA}$ mutant *Tg(kdrl:mCherry)*^{y171} showing separated red channel from panel D. Scale bar: 100 µm.

J. Quantitation of the number of somites with TD segments in wild-type or *shoc2*$^{SA/SA}$ mutants at 5 dpf (n=6 larvae in each group).

K. Quantitation of the number of somites with DLLV segments in wild-type or *shoc2*$^{SA/SA}$ mutants at 5 dpf (n=6 larvae in each group).

L. Quantitation of the number of somites with ISLV in wild-type or *shoc2*$^{SA/SA}$ mutants at 5 dpf (n=6 larvae in each group).

M. Confocal image of the craniofacial lymphatics of a wild-type sibling at 5 dpf. LFL, lateral facial lymphatics, MFL, medial facial lymphatics, OLV, otolithic lymphatic vessel, LAA, lymphatic branchial arches. Scale bar: 100 µm.

N. Confocal image of the craniofacial lymphatics of a *shoc2*$^{SA/SA}$ mutant at 5 dpf. Asterisks indicate the absence of lymphatic vessels. Scale bar: 100 µm.

Figure 2. Defective lymphatic progenitors in shoc2 mutant zebrafish.

A. A schematic showing the region of interest where lymphatic vessels originate. Secondary sprouts emerge from a posterior cardinal vein (PCV) and migrate dorsally around 1.5 dpf, giving rise to the parachordal lines (PL) at 3 dpf. These PLs are lymphatic progenitors that migrate and proliferate to form the trunk lymphatic vessels.

B. Confocal image of trunk vessels of a wild-type sibling *Tg(mrc1a:eGFP)*^{y251}*;Tg(kdrl:mCherry)*^{y171} zebrafish larvae at 32 hpf. The image is converted to a grey scale. Scale bar: 100 µm.

C. Confocal image of trunk vessels of a wild-type sibling *Tg(mrc1a:eGFP)*^{y251}*;Tg(kdrl:mCherry)*^{y171} zebrafish larvae at 41 hpf. The image is converted to a grey scale, and secondary sprouts are pseudocolored in green. Scale bar: 100 µm.

D. Confocal image of trunk vessels of a wild-type sibling *Tg(mrc1a:eGFP)*^{y251}*;Tg(kdrl:mCherry)*^{y171} zebrafish larvae at 50 hpf. The image is converted to a grey scale, and secondary sprouts are pseudocolored in green. Scale bar: 100 µm.

E. Confocal image of trunk vessels of a *shoc2*$^{SA/SA}$ mutant *Tg(mrc1a:eGFP)*^{y251}*;Tg(kdrl:mCherry)*^{y171} zebrafish larvae at 32 hpf. The image is converted to a grey scale. Scale bar: 100 µm.

F. Confocal image of trunk vessels of a *shoc2*$^{SA/SA}$ mutant *Tg(mrc1a:eGFP)*^{y251}*;Tg(kdrl:mCherry)*^{y171} zebrafish larvae at 41 hpf. The image is converted to a greyscale, and secondary sprouts are pseudocolored in green. Scale bar: 100 µm.

G. Confocal image of trunk vessels of a *shoc2*$^{SA/SA}$ mutant *Tg(mrc1a:eGFP)*^{y251}*;Tg(kdrl:mCherry)*^{y171} zebrafish larvae at 50 hpf. The image is converted to a greyscale, and secondary sprouts are pseudocolored in green. Scale bar: 100 µm.

H. Confocal image of trunk vessels of a wild-type sibling *Tg(mrc1a:eGFP)*^{y251}*;Tg(kdrl:mCherry)*^{y171} zebrafish larvae at 3 dpf. PL, parachordal line. Scale bar: 100 µm.

I. Greyscale image of a wild-type sibling *Tg(mrc1a:eGFP)*^{y251}*;Tg(kdrl:mCherry)*^{y171} in panel H. PLs are pseudocolored in green. Scale bar: 100 µm.

J. Confocal image of trunk vessels of a *shoc2*$^{SA/SA}$ mutant *Tg(mrc1a:eGFP)*^{y251}*;Tg(kdrl:mCherry)*^{y171} zebrafish larvae at 3 dpf. Asterisks indicate the absence of PLs. Scale bar: 100 µm.

K. Greyscale image of a *shoc2*$^{SA/SA}$ mutant *Tg(mrc1a:eGFP)*^{y251}*;Tg(kdrl:mCherry)*^{y171} in panel J. Asterisks indicate the absence of PLs. Scale bar: 100 µm.

L. Quantification of the number of somites containing PL segments in wild-type or *shoc2*$^{SA/SA}$ mutants at 3 dpf. Seven somites per larvae were counted (n=7 larvae in each group).

M. Confocal image of trunk vessels of an uninjected *Tg(mrc1a:kalTA4, UAS:eGFP)* zebrafish larvae at 3 dpf. The arrows indicate PLs. Scale bar: 100 µm.

N. Confocal image of trunk vessels of a *Tg(mrc1a:kalTA4, UAS:eGFP)* shoc2 MO-injected zebrafish larvae at 3 dpf. The arrows indicate PLs. Scale bar: 100 µm.

O. Confocal image of trunk vessels of a *Tg(mrc1a:kalTA4, UAS:eGFP)* shoc2 MO and UAS:mCherry co-injected zebrafish larvae at 3 dpf. The arrows indicate PLs. Scale bar: 100 µm.

P. Confocal image of trunk vessels of a *Tg(mrc1a:kalTA4, UAS:eGFP)* shoc2 MO and UAS:mCherry-2A-shoc2 co-injected zebrafish larvae at 3 dpf. The arrows indicate PLs. Scale bar: 100 µm.

Q. Quantification of the number of somites containing PL segments in panels M-P. Ten somites per larvae were counted. Data points indicate the number of larvae in each group.

Figure 3. Shoc2-dependent activation of the ERK1/2 pathway in endothelial cells.

A. Western blot of whole cell lysates extracted from human dermal lymphatic endothelial cells (HDLEC) expressing lentivirally supplied nontargeting shRNA (NT), Shoc2 shRNA (KD) or Shoc2 shRNA together with Shoc2-tagRFP (SE), serum-starved for 16 hr and then stimulated or not with VEGF-C (2 ng/ml) for 7 min at 37ºC. Cell lysates were probed using anti-pERK1/2, -ERK1/2, and -Shoc2 antibodies.

B. Levels of pERK1/2 in cells treated with 2 ng/ml VEGFa at 7 min, normalized to the total amount of ERK1/2 and compared to pERK1/2 levels in parental HDLEC cells expressing nontargeting (NT) treated with 2 ng/ml VEGFa (set at 1.0). Values are shown in arbitrary units ± S.D. (n=3) (*p = 0.01 to 0.05, **p = 0.001 to 0.01, ***p = 0.0001 to 0.001, ****p < 0.0001, ≥ 0.05- non-significant, ns, one-way ANOVA Dunnett's multiple comparison test).

C. Western blot of whole cell lysates extracted from human umbilical vein endothelial cells (HUVEC) expressing lentivirally supplied nontargeting shRNA (NT), Shoc2 shRNA (KD) or Shoc2 shRNA together with Shoc2-tagRFP (SE), serum-starved for 16 hrs and then stimulated or not with VEGF-A (2 ng/ml) for 7 min at 37ºC. Cell lysates were probed using anti-pERK1/2, -ERK1/2, and -Shoc2 antibodies.

D. Levels of pERK1/2 in cells treated with 2 ng/ml VEGFa at 7 min, normalized to the total amount of ERK1/2 and compared to pERK1/2 levels in parental HUVEC cells expressing nontargeting (NT), treated with 2 ng/ml VEGFa (set at 1.0). Values are shown in arbitrary units ± S.D. (n=3) (*p = 0.01 to 0.05, **p = 0.001 to 0.01, ***p = 0.0001 to 0.001, ****p < 0.0001, ≥ 0.05- non-significant, ns, one-way ANOVA Dunnett's multiple comparison test).

E. HDLEC expressing lentivirally-supplied nontargeting shRNA (NT) or Shoc2 shRNA (KD) were stained to examine β-Galactosidase activity (left panels). GFP, expressed independently by the lentivirus, served as a reporter to monitor delivery efficiency (right panels). Scale bar – 150μm.

F. Size distribution of HDLEC expressing lentivirally-supplied nontargeting shRNA (NT) or Shoc2 shRNA (KD), 6 days after transfection, as measured by surface area.

G. Western blot of whole cell lysates extracted from HUVECs and HDLECs expressing lentivirally supplied nontargeting shRNA (NT) or Shoc2 shRNA (KD) for 6 days. Cell lysates were probed using anti-Shoc2, -p53, -53, and -p21 antibodies.

The results in each panel are representative of those from three independent experiments.

Figure 4. The Shoc2-dependent interferon response in HDLEC.

A- B. Gene set enrichment analysis (GSEA) is presented as a score plot with the normalized enrichment score (NES) showing upregulation of interferon (IFN) response signature in Shoc2-depleted HDLEC (Shoc2 KD, KD) compared with control (nontargeting, NT) or HDLEC depleted of endogenous Shoc2 and expressing Shoc2-tagRFP (SE). The total height of the curve indicates the extent of enrichment (ES), with the normalized enrichment score (NES), the false discovery rate (FDR), and the p-value. Source data are provided as a source data file. Heatmap: the top elected correlated genes for each biological triplicate are presented in the corresponding heat map. Red and blue indicate increased and decreased expression for all heatmaps, respectively.

C. The relative GAPDH-normalized expression of selected genes was measured by RT-qPCR. Data represent the mean and standard error of three independent experiments' mean (SEM) values. P-values were calculated using a t-test (*p = 0.01 to 0.05, **p = 0.001 to 0.01, ***p = 0.0001 to 0.001, ****p < 0.0001, ≥ 0.05- non-significant, ns). Black bars represent control (NT), and red bars represent Shoc2-depleted cells (KD).

D. Cell lysates of Shoc2-depleted (KD), control (NT), or Shoc2-tagRFP expressing (SE) HDLEC were analyzed using western blot 3 days and 6 days post-transfection to determine the expression levels of the indicated proteins.

The results in each panel are representative of at least three independent experiments.

Figure 5. **The ERK1/2 pathway-independent activation of the JAK1/STAT1 pathway in Shoc2-depleted HDLEC.**

A. Schematic representation of the major signaling pathway activated by IFNs - the Janus kinase/signal transducer and activator of transcription (JAK1/STAT1) pathway. Activation of the JAK1/STAT1 pathway at the plasma membrane and rapid phosphorylation and nuclear translocation of STAT1 leads to the expression of IFN-stimulated genes (ISGs) containing ISREs or GAS DNA cis-elements.

B. Western blot of whole cell lysates extracted from human dermal lymphatic endothelial cells (HDLEC) expressing lentivirally supplied nontargeting shRNA (NT), Shoc2 shRNA (KD) or Shoc2 shRNA together with Shoc2-tagRFP (SE) for 3 and 6 days. Cell lysates were probed using antibodies to the indicated proteins.

C. Western blot of whole cell lysates extracted from human dermal lymphatic endothelial cells (HDLEC) expressing lentivirally supplied nontargeting shRNA (NT), Shoc2 shRNA (KD) or Shoc2 shRNA together with Shoc2-tagRFP (SE) for 6 days. Cells were treated with 10μM MEK inhibitor PD50042 for 24 hours before western blot. Cell lysates were probed using antibodies to the indicated proteins.

D. Western blot of whole cell lysates extracted from human dermal lymphatic endothelial cells (HDLEC) expressing lentivirally supplied nontargeting shRNA (NT), Shoc2 shRNA (KD) or Shoc2 shRNA together with Shoc2-tagRFP (SE) for 6 days. Cells were treated with 5μM JAK1 inhibitor ruxolitinib for 24 hours before western blot. Cell lysates were probed using antibodies to the indicated proteins.

The results in each panel are representative of at least three independent experiments.

Figure 6. **Cell-specific interferon response in Shoc2-depleted or expressing the Shoc2 S2G NSLH variant HDLEC.**

A. Western blot of whole cell lysates extracted from human dermal lymphatic endothelial cells (HDLEC) expressing lentivirally supplied nontargeting shRNA (NT), Shoc2 shRNA (KD), Shoc2

shRNA together with Shoc2-tagRFP (SE), or Shoc2 shRNA together with Shoc2(S2G)-tagRFP for days. Cell lysates were probed using antibodies to the indicated proteins.

B. Western blot of whole-cell lysates extracted from human vein endothelial cells (HUVEC) expressing lentivirally supplied nontargeting shRNA (NT), Shoc2 shRNA (KD), Shoc2 shRNA together with Shoc2-tagRFP (SE), or Shoc2 shRNA together with Shoc2(S2G)-tagRFP (S2G) for 3 days. Cell lysates were probed using antibodies to the indicated proteins.

The results in each panel are representative of at least three independent experiments.

Figure 7. **Pattern recognition receptor-mediated response in the HDLEC depleted of Shoc2 or expressing the Shoc2 S2G NSLH variant.**

A. Gene set enrichment analysis (GSEA) is presented as a score plot, with NES indicating the upregulation of selected genes in a RIG-1-like signaling signature in Shoc2-depleted HDLEC (Shoc2 KD, KD) compared with the control (nontargeting, NT). The total height of the curve indicates the extent of enrichment (ES), with the normalized enrichment score (NES), the false discovery rate (FDR), and the p-value. Source data are provided as a source data file. Heatmap: the top elected correlated genes for each biological triplicate are presented in the corresponding heat map. Red and blue indicate increased and decreased expression, respectively, for all heatmaps.

B. Schematic representation of the RIG-I/MDA5 nucleic acid sensing pathway activated by dsRNA. Activation of MDA5 and its interaction with MAVS leads to phosphorylation of the transcription factors IRF7 and IRF9, ensuring their translocation into the nucleus, where they drive the expression of the IFN genes.

C. The relative GAPDH-normalized expression of selected genes was measured by RT-qPCR. Data represent the mean and standard error of three independent experiments' mean (SEM) values. P-values were calculated using a *t*-test (*p = 0.01 to 0.05, **p = 0.001 to 0.01, ***p = 0.0001 to 0.001, ****p < 0.0001, ≥ 0.05- non-significant, ns). Black bars represent control (NT), and red bars represent Shoc2-depleted cells (KD).

D. MDA5 was precipitated from HDLEC cells depleted of Shoc2 (KD), control (NT), expressing Shoc2-tagRFP (SE), or the Shoc2 S2G variants using anti-MDA5 antibodies. Immunoblots were analyzed with anti-pMDA5 (Ser88), anti-MDA5, and anti-GAPDH antibodies.

E. MDA5 was precipitated from HUVEC cells depleted of Shoc2 (KD), control (NT), expressing Shoc2-tagRFP (SE), or the Shoc2 S2G variants using anti-MDA5 antibodies. Immunoblots were analyzed using anti-pMDA5 (Ser88), MDA5, and GAPDH antibodies.

F. Western blot of whole-cell lysates extracted from HDLEC cells expressing lentivirally supplied nontargeting shRNA (NT), Shoc2 shRNA (KD), and transfected with the indicated siRNAs. Cell lysates were probed using antibodies to the indicated proteins.

The results in each panel are representative of at least three independent experiments.

Figure 8. Mitochondrial changes in Shoc2-depleted HDLEC

A. Western blot of whole-cell lysates extracted from HDLEC expressing lentivirally supplied nontargeting shRNA (NT), Shoc2 shRNA (KD), Shoc2 shRNA together with Shoc2-tagRFP (SE), or Shoc2 shRNA together with Shoc2(S2G)-tagRFP (S2G) for 3 and 6 days. Cell lysates were probed using antibodies relevant to mitochondrial fission and fusion. GAPDH was used as a loading control.

B. Relative oxygen consumption rate (OCR), measured by the Seahorse XFe96 analyzer, is normalized to cell number. Data are presented as mean ± SEM of three independent experiments. Statistical significance was determined by one-way ANOVA (brown Forysthe), Dunnett's multiple comparisons test (*p = 0.01 to 0.05, **p = 0.001 to 0.01, ***p = 0.0001 to 0.001, ****p < 0.0001, ≥ 0.05- non-significant, ns). FCCP, carbonyl cyanide-*p* trifluoromethoxyphenylhydrazone; Rot, rotenone; AA, antimycin A.

C-F. Basal and maximal OCR analysis, Mitochondrial ATP production, and proton leak of HDLEC depleted of Shoc2 (KD) or expressing either Shoc2-tagRFP (SE) or Shoc2-tagRFP S2G (S2G). Statistical significance was determined by one-way ANOVA (brown Forysthe), Dunnett's multiple comparisons test (*p = 0.01 to 0.05, **p = 0.001 to 0.01, ***p = 0.0001 to 0.001, ****p < 0.0001, ≥ 0.05- non-significant, ns).

Figure 9. Shoc2 controls mTOR pathway activation in HDLEC.

A. Schematic representation of the Shoc2-mTOR axis in which Raptor binding to mTOR stimulates mTORC1 complex activity indicated by S6K and 4EBP phosphorylation. mTORC1 activation is followed by activation of the IFN/Jak/STAT response.

B. Western blot of whole cell lysates extracted from HDLEC expressing lentivirally supplied nontargeting shRNA (NT), Shoc2 shRNA (KD), Shoc2 shRNA together with Shoc2-tagRFP (SE), or

Shoc2 shRNA together with Shoc2(S2G)-tagRFP (S2G) for 3 days. Cell lysates were probed using antibodies to proteins relevant to mTORC1 signaling. GAPDH was used as a loading control.

C. Cell lysates were prepared from HDLEC cells expressing lentivirally supplied nontargeting shRNA (NT), Shoc2 shRNA (KD), Shoc2 shRNA together with Shoc2-tagRFP (SE), or Shoc2 shRNA together with Shoc2(S2G)-tagRFP (S2G) for 3 days. mTOR was immunoprecipitated with an anti-mTOR antibody. Immunoprecipitated proteins were subjected to SDS-PAGE and western blot analysis. Blots were probed with antibodies against mTOR, Raptor, and Rictor.

D. Western blot of whole cell lysates extracted from HUVEC expressing lentivirally supplied nontargeting shRNA (NT), Shoc2 shRNA (KD), Shoc2 shRNA together with Shoc2-tagRFP (SE), or Shoc2 shRNA together with Shoc2(S2G)-tagRFP (S2G) for 3 days. Cell lysates were probed using antibodies to proteins relevant to mTORC1 signaling. GAPDH was used as a loading control.

E. Cell lysates were prepared from HUVEC cells expressing lentivirally supplied nontargeting shRNA (NT), Shoc2 shRNA (KD), Shoc2 shRNA together with Shoc2-tagRFP (SE), or Shoc2 shRNA together with Shoc2(S2G)-tagRFP (S2G) for 3 days. mTOR was immunoprecipitated with an anti-mTOR antibody. Immunoprecipitated proteins were subjected to SDS-PAGE and western blot analysis. Blots were probed with antibodies against mTOR, Raptor, and Rictor.

F. Western blot of whole cell lysates extracted from HDLEC expressing lentivirally supplied nontargeting shRNA (NT), Shoc2 shRNA (KD), Shoc2 shRNA together with Shoc2-tagRFP (SE), or Shoc2 shRNA together with Shoc2(S2G)-tagRFP (S2G) for 3 days and treated with Rapamycin. Cell lysates were probed using the indicated antibodies. GAPDH was used as a loading control.

G. Schematic showing the working model depicting what is currently understood for the mechanisms by which Shoc2 modulates HDLEC homeostasis. Shoc2 prevents excessive activation of the mTORC1 complex. Shoc2 loss leads to increased Raptor binding to mTOR, increased mTORC1 signaling, mitochondrial fission, and potential leak of mitochondrial double-stranded RNA. Mt-dsRNAs then trigger an innate immune response, initiating sterile inflammation.

REFERENCES

1. Hu, Z., Zhao, X., Wu, Z., Qu, B., Yuan, M., Xing, Y., Song, Y., and Wang, Z. (2024). Lymphatic vessel: Origin, heterogeneity, biological functions and therapeutic targets. Signal Transduction and Targeted Therapy *9*, 9. 10.1038/s41392-023-01723-x.
2. Petrova, T.V., and Koh, G.Y. (2020). Biological functions of lymphatic vessels. Science *369*. 10.1126/science.aax4063.
3. Oliver, G., Kipnis, J., Randolph, G.J., and Harvey, N.L. (2020). The Lymphatic Vasculature in the 21(st) Century: Novel Functional Roles in Homeostasis and Disease. Cell *182*, 270-296. 10.1016/j.cell.2020.06.039.
4. Stritt, S., Koltowska, K., and Makinen, T. (2021). Homeostatic maintenance of the lymphatic vasculature. Trends Mol Med *27*, 955-970. 10.1016/j.molmed.2021.07.003.
5. Ricard, N., Bailly, S., Guignabert, C., and Simons, M. (2021). The quiescent endothelium: signalling pathways regulating organ-specific endothelial normalcy. Nat Rev Cardiol *18*, 565-580. 10.1038/s41569-021-00517-4.
6. Bui, K., and Hong, Y.K. (2020). Ras Pathways on Prox1 and Lymphangiogenesis: Insights for Therapeutics. Front Cardiovasc Med *7*, 597374. 10.3389/fcvm.2020.597374.
7. Deng, Y., Atri, D., Eichmann, A., and Simons, M. (2013). Endothelial ERK signaling controls lymphatic fate specification. J Clin Invest *123*, 1202-1215. 10.1172/JCI63034.
8. Yu, P., Tung, J.K., and Simons, M. (2014). Lymphatic fate specification: an ERK-controlled transcriptional program. Microvasc Res *96*, 10-15. 10.1016/j.mvr.2014.07.016.
9. Meng, Y., Lv, T., Zhang, J., Shen, W., Li, L., Li, Y., Liu, X., Lei, X., Lin, X., Xu, H., et al. (2023). Temporospatial inhibition of Erk signaling is required for lymphatic valve formation. Signal Transduction and Targeted Therapy *8*, 342. 10.1038/s41392-023-01571-9.
10. Tidyman, W.E., and Rauen, K.A. (2016). Pathogenetics of the RASopathies. Hum Mol Genet *25*, R123-R132. 10.1093/hmg/ddw191.
11. Zenker, M. (2022). Clinical overview on RASopathies. Am J Med Genet C Semin Med Genet. 10.1002/ajmg.c.32015.
12. https://rarediseases.org/rare-diseases/noonan-syndrome/.
13. Chen, C.P. (2024). Syndromic and single gene disorders associated with fetal pleural effusion (I): Noonan syndrome, RASopathy and congenital lymphatic anomalies. Taiwan J Obstet Gynecol *63*, 174-177. 10.1016/j.tjog.2024.01.011.
14. Kleimeier, L.E.R., van Schaik, C., Leenders, E., Itkin, M., Klein, W.M., and Draaisma, J.M.T. (2022). Lymphatic Phenotype of Noonan Syndrome: Innovative Diagnosis and Possible Implications for Therapy. J Clin Med *11*. 10.3390/jcm11113128.
15. Mazzanti, L., Cacciari, E., Cicognani, A., Bergamaschi, R., Scarano, E., and Forabosco, A. (2003). Noonan-like syndrome with loose anagen hair: a new syndrome? Am J Med Genet A *118A*, 279-286. 10.1002/ajmg.a.10923.
16. Cordeddu, V., Di Schiavi, E., Pennacchio, L.A., Ma'ayan, A., Sarkozy, A., Fodale, V., Cecchetti, S., Cardinale, A., Martin, J., Schackwitz, W., et al. (2009). Mutation of SHOC2 promotes aberrant protein N-myristoylation and causes Noonan-like syndrome with loose anagen hair. Nat Genet *41*, 1022-1026. 10.1038/ng.425.
17. Hannig, V., Jeoung, M., Jang, E.R., Phillips, J.A., 3rd, and Galperin, E. (2014). A Novel SHOC2 Variant in Rasopathy. Hum Mutat *35*, 1290-1294. 10.1002/humu.22634.

18. Baldassarre, G., Mussa, A., Banaudi, E., Rossi, C., Tartaglia, M., Silengo, M., and Ferrero, G.B. (2014). Phenotypic variability associated with the invariant SHOC2 c.4A>G (p.Ser2Gly) missense mutation. Am J Med Genet A *164A*, 3120-3125. 10.1002/ajmg.a.36697.
19. Garavelli, L., Cordeddu, V., Errico, S., Bertolini, P., Street, M.E., Rosato, S., Pollazzon, M., Wischmeijer, A., Ivanovski, I., Daniele, P., et al. (2015). Noonan syndrome-like disorder with loose anagen hair: a second case with neuroblastoma. Am J Med Genet A *167A*, 1902-1907. 10.1002/ajmg.a.37082.
20. Gargano, G., Guidotti, I., Balestri, E., Vagnarelli, F., Rosato, S., Comitini, G., Wischmeijer, A., La Sala, G.B., Iughetti, L., Cordeddu, V., et al. (2014). Hydrops fetalis in a preterm newborn heterozygous for the c.4A>G SHOC2 mutation. Am J Med Genet A *164A*, 1015-1020. 10.1002/ajmg.a.36376.
21. Motta, M., Solman, M., Bonnard, A.A., Kuechler, A., Pantaleoni, F., Priolo, M., Chandramouli, B., Coppola, S., Pizzi, S., Zara, E., et al. (2022). Expanding the molecular spectrum of pathogenic SHOC2 variants underlying Mazzanti syndrome. Hum Mol Genet *31*, 2766-2778. 10.1093/hmg/ddac071.
22. Digilio, M.C., Lepri, F., Baban, A., Dentici, M.L., Versacci, P., Capolino, R., Ferese, R., De Luca, A., Tartaglia, M., Marino, B., and Dallapiccola, B. (2011). RASopathies: Clinical Diagnosis in the First Year of Life. Mol Syndromol *1*, 282-289. 10.1159/000331266.
23. Gargano, G., Guidotti, I., Balestri, E., Vagnarelli, F., Rosato, S., Comitini, G., Wischmeijer, A., La Sala, G.B., Iughetti, L., Cordeddu, V., et al. (2014). Hydrops fetalis in a preterm newborn heterozygous for the c.4A>G SHOC2 mutation. Am J Med Genet A. 10.1002/ajmg.a.36376.
24. Zmolikova, M., Puchmajerova, A., Hecht, P., Lebl, J., Trkova, M., and Krepelova, A. (2014). Coarctation of the aorta in Noonan-like syndrome with loose anagen hair. Am J Med Genet A *164A*, 1218-1221. 10.1002/ajmg.a.36404.
25. Jang, H., Stevens, P., Gao, T., and Galperin, E. (2021). The leucine-rich repeat signaling scaffolds Shoc2 and Erbin: cellular mechanism and role in disease. FEBS J *288*, 721-739. 10.1111/febs.15450.
26. Rodriguez-Viciana, P., Oses-Prieto, J., Burlingame, A., Fried, M., and McCormick, F. (2006). A phosphatase holoenzyme comprised of Shoc2/Sur8 and the catalytic subunit of PP1 functions as an M-Ras effector to modulate Raf activity. Mol Cell *22*, 217-230. 10.1016/j.molcel.2006.03.027.
27. Wilson, P., Abdelmoti, L., Norcross, R., Jang, E.R., Palayam, M., and Galperin, E. (2021). The role of USP7 in the Shoc2-ERK1/2 signaling axis and Noonan-like syndrome with loose anagen hair. Journal of cell science *134*. 10.1242/jcs.258922.
28. Xie, C.M., Tan, M., Lin, X.T., Wu, D., Jiang, Y., Tan, Y., Li, H., Ma, Y., Xiong, X., and Sun, Y. (2019). The FBXW7-SHOC2-Raptor Axis Controls the Cross-Talks between the RAS-ERK and mTORC1 Signaling Pathways. Cell reports *26*, 3037-3050 e3034. 10.1016/j.celrep.2019.02.052.
29. Jang, E.R., Shi, P., Bryant, J., Chen, J., Dukhande, V., Gentry, M.S., Jang, H., Jeoung, M., and Galperin, E. (2014). HUWE1 is a molecular link controlling RAF-1 activity supported by the Shoc2 scaffold. Mol Cell Biol *34*, 3579-3593. 10.1128/MCB.00811-14.
30. Jang, E.R., Jang, H., Shi, P., Popa, G., Jeoung, M., and Galperin, E. (2015). Spatial control of Shoc2-scaffold-mediated ERK1/2 signaling requires remodeling activity of the ATPase PSMC5. J Cell Sci *128*, 4428-4441. 10.1242/jcs.177543.
31. Jang, H., Jang, E.R., Wilson, P.G., Anderson, D., and Galperin, E. (2019). VCP/p97 controls signals of the ERK1/2 pathway transmitted via the Shoc2 scaffolding complex: novel insights into IBMPFD pathology. Mol Biol Cell *30*, 1655-1663. 10.1091/mbc.E19-03-0144.

32. Jang, E.R., and Galperin, E. (2016). The function of Shoc2: A scaffold and beyond. Communicative & integrative biology *9*, e1188241. 10.1080/19420889.2016.1188241.
33. Xie, C.M., and Sun, Y. (2019). The MTORC1-mediated autophagy is regulated by the FBXW7-SHOC2-RPTOR axis. Autophagy *15*, 1470-1472. 10.1080/15548627.2019.1609864.
34. Kaduwal, S., Jeong, W.J., Park, J.C., Lee, K.H., Lee, Y.M., Jeon, S.H., Lim, Y.B., Min do, S., and Choi, K.Y. (2015). Sur8/Shoc2 promotes cell motility and metastasis through activation of Ras-PI3K signaling. Oncotarget *6*, 33091-33105. 10.18632/oncotarget.5173.
35. Norcross, R.G., Abdelmoti, L., Rouchka, E.C., Andreeva, K., Tussey, O., Landestoy, D., and Galperin, E. (2022). Shoc2 controls ERK1/2-driven neural crest development by balancing components of the extracellular matrix. Dev Biol *492*, 156-171. 10.1016/j.ydbio.2022.10.010.
36. Jang, H., Oakley, E., Forbes-Osborne, M., Kesler, M.V., Norcross, R., Morris, A.C., and Galperin, E. (2019). Hematopoietic and neural crest defects in zebrafish shoc2 mutants: a novel vertebrate model for Noonan-like syndrome. Hum Mol Genet *28*, 501-514. 10.1093/hmg/ddy366.
37. Yi, J., Chen, M., Wu, X., Yang, X., Xu, T., Zhuang, Y., Han, M., and Xu, R. (2010). Endothelial SUR-8 acts in an ERK-independent pathway during atrioventricular cushion development. Dev Dyn *239*, 2005-2013. 10.1002/dvdy.22343.
38. Yi, J., Chen, M., Wu, X., Yang, X., Xu, T., Zhuang, Y., Han, M., and Xu, R. (2010). Endothelial SUR-8 acts in an ERK-independent pathway during atrioventricular cushion development. Dev Dyn *239*, 2005-2013. 10.1002/dvdy.22343.
39. Yaniv, K., Isogai, S., Castranova, D., Dye, L., Hitomi, J., and Weinstein, B.M. (2007). Imaging the developing lymphatic system using the zebrafish. Novartis Found Symp *283*, 139-148; discussion 148-151, 238-141. 10.1002/9780470319413.ch11.
40. Jung, H.M., Castranova, D., Swift, M.R., Pham, V.N., Venero Galanternik, M., Isogai, S., Butler, M.G., Mulligan, T.S., and Weinstein, B.M. (2017). Development of the larval lymphatic system in zebrafish. Development *144*, 2070-2081. 10.1242/dev.145755.
41. Yaniv, K., Isogai, S., Castranova, D., Dye, L., Hitomi, J., and Weinstein, B.M. (2006). Live imaging of lymphatic development in the zebrafish. Nat Med *12*, 711-716. 10.1038/nm1427.
42. Cha, Y.R., Fujita, M., Butler, M., Isogai, S., Kochhan, E., Siekmann, A.F., and Weinstein, B.M. (2012). Chemokine signaling directs trunk lymphatic network formation along the preexisting blood vasculature. Dev Cell *22*, 824-836. 10.1016/j.devcel.2012.01.011.
43. He, S., and Sharpless, N.E. (2017). Senescence in Health and Disease. Cell *169*, 1000-1011. 10.1016/j.cell.2017.05.015.
44. Diamond, M.S., and Farzan, M. (2013). The broad-spectrum antiviral functions of IFIT and IFITM proteins. Nat Rev Immunol *13*, 46-57. 10.1038/nri3344.
45. Kang, J.A., Kim, Y.J., and Jeon, Y.J. (2022). The diverse repertoire of ISG15: more intricate than initially thought. Experimental & Molecular Medicine *54*, 1779-1792. 10.1038/s12276-022-00872-3.
46. Bluyssen, H.A., Vlietstra, R.J., van der Made, A., and Trapman, J. (1994). The interferon-stimulated gene 54 K promoter contains two adjacent functional interferon-stimulated response elements of different strength, which act synergistically for maximal interferon-alpha inducibility. Eur J Biochem *220*, 395-402. 10.1111/j.1432-1033.1994.tb18636.x.
47. Ronni, T., Matikainen, S., Lehtonen, A., Palvimo, J., Dellis, J., Van Eylen, F., Goetschy, J.F., Horisberger, M., Content, J., and Julkunen, I. (1998). The proximal interferon-stimulated response elements are essential for interferon responsiveness: a promoter analysis of the antiviral MxA gene. J Interferon Cytokine Res *18*, 773-781. 10.1089/jir.1998.18.773.

48. Ohtomo, T., Sugamata, Y., Ozaki, Y., Ono, K., Yoshimura, Y., Kawai, S., Koishihara, Y., Ozaki, S., Kosaka, M., Hirano, T., and Tsuchiya, M. (1999). Molecular cloning and characterization of a surface antigen preferentially overexpressed on multiple myeloma cells. Biochem Biophys Res Commun *258*, 583-591. 10.1006/bbrc.1999.0683.
49. Farlik, M., Rapp, B., Marie, I., Levy, D.E., Jamieson, A.M., and Decker, T. (2012). Contribution of a TANK-binding kinase 1-interferon (IFN) regulatory factor 7 pathway to IFN-γ-induced gene expression. Mol Cell Biol *32*, 1032-1043. 10.1128/mcb.06021-11.
50. Platanias, L.C. (2005). Mechanisms of type-I- and type-II-interferon-mediated signalling. Nat Rev Immunol *5*, 375-386. 10.1038/nri1604.
51. Ko, C.Y., Chang, W.C., and Wang, J.M. (2015). Biological roles of CCAAT/Enhancer-binding protein delta during inflammation. J Biomed Sci *22*, 6. 10.1186/s12929-014-0110-2.
52. Hu, J., Roy, S.K., Shapiro, P.S., Rodig, S.R., Reddy, S.P., Platanias, L.C., Schreiber, R.D., and Kalvakolanu, D.V. (2001). ERK1 and ERK2 activate CCAAAT/enhancer-binding protein-beta-dependent gene transcription in response to interferon-gamma. J Biol Chem *276*, 287-297. 10.1074/jbc.M004885200.
53. Stivala, S., Codilupi, T., Brkic, S., Baerenwaldt, A., Ghosh, N., Hao-Shen, H., Dirnhofer, S., Dettmer, M.S., Simillion, C., Kaufmann, B.A., et al. (2019). Targeting compensatory MEK/ERK activation increases JAK inhibitor efficacy in myeloproliferative neoplasms. J Clin Invest *129*, 1596-1611. 10.1172/jci98785.
54. Reikine, S., Nguyen, J.B., and Modis, Y. (2014). Pattern Recognition and Signaling Mechanisms of RIG-I and MDA5. Front Immunol *5*, 342. 10.3389/fimmu.2014.00342.
55. Wies, E., Wang, M.K., Maharaj, N.P., Chen, K., Zhou, S., Finberg, R.W., and Gack, M.U. (2013). Dephosphorylation of the RNA sensors RIG-I and MDA5 by the phosphatase PP1 is essential for innate immune signaling. Immunity *38*, 437-449. 10.1016/j.immuni.2012.11.018.
56. Liu, G., Lee, J.H., Parker, Z.M., Acharya, D., Chiang, J.J., van Gent, M., Riedl, W., Davis-Gardner, M.E., Wies, E., Chiang, C., and Gack, M.U. (2021). ISG15-dependent activation of the sensor MDA5 is antagonized by the SARS-CoV-2 papain-like protease to evade host innate immunity. Nat Microbiol *6*, 467-478. 10.1038/s41564-021-00884-1.
57. Refolo, G., Vescovo, T., Piacentini, M., Fimia, G.M., and Ciccosanti, F. (2020). Mitochondrial Interactome: A Focus on Antiviral Signaling Pathways. Front Cell Dev Biol *8*, 8. 10.3389/fcell.2020.00008.
58. Sun, X., Sun, L., Zhao, Y., Li, Y., Lin, W., Chen, D., and Sun, Q. (2016). MAVS maintains mitochondrial homeostasis via autophagy. Cell Discovery *2*, 16024. 10.1038/celldisc.2016.24.
59. Marques, E., Kramer, R., and Ryan, D.G. (2024). Multifaceted mitochondria in innate immunity. NPJ Metab Health Dis *2*, 6. 10.1038/s44324-024-00008-3.
60. Xie, C.M., and Sun, Y. (2019). The MTORC1-mediated autophagy is regulated by the FBXW7-SHOC2-RPTOR axis. Autophagy, 1-3. 10.1080/15548627.2019.1609864.
61. Lapinski, P.E., Lubeck, B.A., Chen, D., Doosti, A., Zawieja, S.D., Davis, M.J., and King, P.D. (2017). RASA1 regulates the function of lymphatic vessel valves in mice. J Clin Invest *127*, 2569-2585. 10.1172/jci89607.
62. Norcross, R.G., and Abdelmoti, L., Rouchka, E. C., Andreeva, K. Tussey, O. Landestoy, D. Galperin, E. (2022). Shoc2 controls ERK1/2-driven neural crest development by balancing components of the extracellular matrix. Developmental biology.
63. Bonsor, D.A., and Simanshu, D.K. (2024). RAS and SHOC2 Roles in RAF Activation and Therapeutic Considerations. Annu Rev Cancer Biol *8*, 97-113. 10.1146/annurev-cancerbio-062822-030450.

64. Terai, H., Hamamoto, J., Emoto, K., Masuda, T., Manabe, T., Kuronuma, S., Kobayashi, K., Masuzawa, K., Ikemura, S., Nakayama, S., et al. (2021). SHOC2 Is a Critical Modulator of Sensitivity to EGFR-TKIs in Non-Small Cell Lung Cancer Cells. Mol Cancer Res *19*, 317-328. 10.1158/1541-7786.MCR-20-0664.
65. Sulahian, R., Kwon, J.J., Walsh, K.H., Pailler, E., Bosse, T.L., Thaker, M., Almanza, D., Dempster, J.M., Pan, J., Piccioni, F., et al. (2019). Synthetic Lethal Interaction of SHOC2 Depletion with MEK Inhibition in RAS-Driven Cancers. Cell reports *29*, 118-134 e118. 10.1016/j.celrep.2019.08.090.
66. You, X., Dou, L., Tan, M., Xiong, X., and Sun, Y. (2024). SHOC2 plays an oncogenic or tumor-suppressive role by differentially targeting the MAPK and mTORC1 signals in liver cancer. Life Medicine *3*. 10.1093/lifemedi/lnae023.
67. Yu, B., Ma, J., Li, J., Wang, D., Wang, Z., and Wang, S. (2020). Mitochondrial phosphatase PGAM5 modulates cellular senescence by regulating mitochondrial dynamics. Nat Commun *11*, 2549. 10.1038/s41467-020-16312-7.
68. Chen, W., Zhao, H., and Li, Y. (2023). Mitochondrial dynamics in health and disease: mechanisms and potential targets. Signal Transduction and Targeted Therapy *8*, 333. 10.1038/s41392-023-01547-9.
69. Carroll, B., Nelson, G., Rabanal-Ruiz, Y., Kucheryavenko, O., Dunhill-Turner, N.A., Chesterman, C.C., Zahari, Q., Zhang, T., Conduit, S.E., Mitchell, C.A., et al. (2017). Persistent mTORC1 signaling in cell senescence results from defects in amino acid and growth factor sensing. J Cell Biol *216*, 1949-1957. 10.1083/jcb.201610113.
70. de la Cruz López, K.G., Toledo Guzmán, M.E., Sánchez, E.O., and García Carrancá, A. (2019). mTORC1 as a Regulator of Mitochondrial Functions and a Therapeutic Target in Cancer. Frontiers in Oncology *9*. 10.3389/fonc.2019.01373.
71. Morita, M., Prudent, J., Basu, K., Goyon, V., Katsumura, S., Hulea, L., Pearl, D., Siddiqui, N., Strack, S., McGuirk, S., et al. (2017). mTOR Controls Mitochondrial Dynamics and Cell Survival via MTFP1. Mol Cell *67*, 922-935.e925. 10.1016/j.molcel.2017.08.013.
72. Yoon, J., Kim, S., Lee, M., and Kim, Y. (2023). Mitochondrial nucleic acids in innate immunity and beyond. Exp Mol Med *55*, 2508-2518. 10.1038/s12276-023-01121-x.
73. Shao, X., and Liu, C. (2006). Influence of IFN- alpha and IFN- gamma on lymphangiogenesis. J Interferon Cytokine Res *26*, 568-574. 10.1089/jir.2006.26.568.
74. Kemp, S.S., Penn, M.R., Koller, G.M., Griffin, C.T., and Davis, G.E. (2022). Proinflammatory mediators, TNFalpha, IFNgamma, and thrombin, directly induce lymphatic capillary tube regression. Front Cell Dev Biol *10*, 937982. 10.3389/fcell.2022.937982.
75. Lucas, E.D., and Tamburini, B.A.J. (2019). Lymph Node Lymphatic Endothelial Cell Expansion and Contraction and the Programming of the Immune Response. Front Immunol *10*, 36. 10.3389/fimmu.2019.00036.
76. Grant, S.M., Lou, M., Yao, L., Germain, R.N., and Radtke, A.J. (2020). The lymph node at a glance - how spatial organization optimizes the immune response. J Cell Sci *133*. 10.1242/jcs.241828.
77. Embry, A., Baggett, N.S., Heisler, D.B., White, A., de Jong, M.F., Kocsis, B.L., Tomchick, D.R., Alto, N.M., and Gammon, D.B. (2024). Exploiting bacterial effector proteins to uncover evolutionarily conserved antiviral host machinery. PLoS Pathog *20*, e1012010. 10.1371/journal.ppat.1012010.

78. Zhao, B.R., Wang, X.X., and Wang, X.W. (2022). Shoc2 recognizes bacterial flagellin and mediates antibacterial Erk/Stat signaling in an invertebrate. PLoS Pathog *18*, e1010253. 10.1371/journal.ppat.1010253.
79. Cordeddu, V., Di Schiavi, E., Pennacchio, L.A., Ma'ayan, A., Sarkozy, A., Fodale, V., Cecchetti, S., Cardinale, A., Martin, J., Schackwitz, W., et al. (2009). Mutation of SHOC2 promotes aberrant protein N-myristoylation and causes Noonan-like syndrome with loose anagen hair. Nat Genet *41*, 1022-1026. 10.1038/ng.425.
80. Dard, L., Bellance, N., Lacombe, D., and Rossignol, R. (2018). RAS signalling in energy metabolism and rare human diseases. Biochim Biophys Acta Bioenerg *1859*, 845-867. 10.1016/j.bbabio.2018.05.003.
81. Dard, L., Blanchard, W., Hubert, C., Lacombe, D., and Rossignol, R. (2020). Mitochondrial functions and rare diseases. Mol Aspects Med *71*, 100842. 10.1016/j.mam.2019.100842.
82. Dard, L., Hubert, C., Esteves, P., Blanchard, W., Bou About, G., Baldasseroni, L., Dumon, E., Angelini, C., Delourme, M., Guyonnet-Duperat, V., et al. (2022). HRAS germline mutations impair LKB1/AMPK signaling and mitochondrial homeostasis in Costello syndrome models. J Clin Invest *132*. 10.1172/JCI131053.
83. Bajia, D., Bottani, E., and Derwich, K. (2022). Effects of Noonan Syndrome-Germline Mutations on Mitochondria and Energy Metabolism. Cells *11*. 10.3390/cells11193099.
84. Lee, I., Pecinova, A., Pecina, P., Neel, B.G., Araki, T., Kucherlapati, R., Roberts, A.E., and Huttemann, M. (2010). A suggested role for mitochondria in Noonan syndrome. Biochim Biophys Acta *1802*, 275-283. 10.1016/j.bbadis.2009.10.005.
85. Zhang, E.E., Chapeau, E., Hagihara, K., and Feng, G.S. (2004). Neuronal Shp2 tyrosine phosphatase controls energy balance and metabolism. Proc Natl Acad Sci U S A *101*, 16064-16069. 10.1073/pnas.0405041101.
86. Kleefstra, T., Wortmann, S.B., Rodenburg, R.J., Bongers, E.M., Hadzsiev, K., Noordam, C., van den Heuvel, L.P., Nillesen, W.M., Hollody, K., Gillessen-Kaesbach, G., et al. (2011). Mitochondrial dysfunction and organic aciduria in five patients carrying mutations in the Ras-MAPK pathway. Eur J Hum Genet *19*, 138-144. 10.1038/ejhg.2010.171.
87. Rigante, D., Leoni, C., Onesimo, R., Giorgio, V., Trevisan, V., and Zampino, G. (2023). Aberrant N-myristoylation as a prelude to autoimmune manifestations in patients with SHOC2 mutations. Autoimmun Rev *22*, 103462. 10.1016/j.autrev.2023.103462.
88. Quaio, C.R., Carvalho, J.F., da Silva, C.A., Bueno, C., Brasil, A.S., Pereira, A.C., Jorge, A.A., Malaquias, A.C., Kim, C.A., and Bertola, D.R. (2012). Autoimmune disease and multiple autoantibodies in 42 patients with RASopathies. Am J Med Genet A *158A*, 1077-1082. 10.1002/ajmg.a.35290.
89. Siano, M.A., Marchetti, V., Pagano, S., Di Candia, F., Alessio, M., De Brasi, D., De Luca, A., Pinna, V., Sestito, S., Concolino, D., et al. (2021). Risk of autoimmune diseases in patients with RASopathies: systematic study of humoral and cellular immunity. Orphanet J Rare Dis *16*, 410. 10.1186/s13023-021-02050-6.
90. Bader-Meunier, B., Cave, H., Jeremiah, N., Magerus, A., Lanzarotti, N., Rieux-Laucat, F., and Cormier-Daire, V. (2013). Are RASopathies new monogenic predisposing conditions to the development of systemic lupus erythematosus? Case report and systematic review of the literature. Semin Arthritis Rheum *43*, 217-219. 10.1016/j.semarthrit.2013.04.009.
91. Wang, X.O., Liu, Z.Q., Shangguan, S.F., Lai, J.M., Wang, P.C., Song, F.Y., Ye, X., Du, M., Huang, S.Y., and Gao, K. (2025). [Clinical characteristics analysis of children with Noonan-like

syndrome with loose anagen hair]. Zhonghua Er Ke Za Zhi *63*, 405-410. 10.3760/cma.j.cn112140-20241010-00706.
92. Menentoğlu, B., Konur Akbaş, E.N., Kavrul Kayaalp, G., Akgün, Ö., Aslanger, A.D., Uyguner, Z.O., and Aktay Ayaz, N. (2025). Complex crosstalk: early-onset lupus and antiphospholipid syndrome in a child with SHOC2 related RASopathy. Rheumatology (Oxford). 10.1093/rheumatology/keaf144.
93. Okazaki, T., Saito, Y., Sugita, K., Nosaka, K., Ohno, K., Hiraoka, Y., Kasagi, N., Ebiki, M., Narai, S., Kawashima, Y., et al. (2019). Recurrent Erythema Nodosum in a Child with a SHOC2 Gene Mutation. Yonago acta medica *62*, 159-162.
94. Jeoung, M., Abdelmoti, L., Jang, E.R., Vander Kooi, C.W., and Galperin, E. (2013). Functional Integration of the Conserved Domains of Shoc2 Scaffold. PLoS One *8*, e66067. 10.1371/journal.pone.0066067.
95. Jeoung, M., and Galperin, E. (2014). Visualizing of signaling proteins on endosomes utilizing knockdown and reconstitution approach. Methods Enzymol *534*, 47-63. 10.1016/B978-0-12-397926-1.00003-2.
96. Kimmel, C.B., Ballard, W.W., Kimmel, S.R., Ullmann, B., and Schilling, T.F. (1995). Stages of embryonic development of the zebrafish. Developmental dynamics : an official publication of the American Association of Anatomists *203*, 253-310. 10.1002/aja.1002030302.
97. Fujita, M., Cha, Y.R., Pham, V.N., Sakurai, A., Roman, B.L., Gutkind, J.S., and Weinstein, B.M. (2011). Assembly and patterning of the vascular network of the vertebrate hindbrain. Development *138*, 1705-1715. 10.1242/dev.058776.
98. Lawson, N.D., and Weinstein, B.M. (2002). In vivo imaging of embryonic vascular development using transgenic zebrafish. Dev Biol *248*, 307-318. 10.1006/dbio.2002.0711.
99. Kwan, K.M., Fujimoto, E., Grabher, C., Mangum, B.D., Hardy, M.E., Campbell, D.S., Parant, J.M., Yost, H.J., Kanki, J.P., and Chien, C.B. (2007). The Tol2kit: a multisite gateway-based construction kit for Tol2 transposon transgenesis constructs. Developmental dynamics : an official publication of the American Association of Anatomists *236*, 3088-3099. 10.1002/dvdy.21343.
100. Jung, H.M., Isogai, S., Kamei, M., Castranova, D., Gore, A.V., and Weinstein, B.M. (2016). Imaging blood vessels and lymphatic vessels in the zebrafish. Methods Cell Biol *133*, 69-103. 10.1016/bs.mcb.2016.03.023.
101. Bolger, A.M., Lohse, M., and Usadel, B. (2014). Trimmomatic: a flexible trimmer for Illumina sequence data. Bioinformatics *30*, 2114-2120. 10.1093/bioinformatics/btu170.
102. Li, B., and Dewey, C.N. (2011). RSEM: accurate transcript quantification from RNA-Seq data with or without a reference genome. BMC Bioinformatics *12*, 323. 10.1186/1471-2105-12-323.
103. Robinson, M.D., McCarthy, D.J., and Smyth, G.K. (2010). edgeR: a Bioconductor package for differential expression analysis of digital gene expression data. Bioinformatics *26*, 139-140. 10.1093/bioinformatics/btp616.
104. Subramanian, A., Tamayo, P., Mootha, V.K., Mukherjee, S., Ebert, B.L., Gillette, M.A., Paulovich, A., Pomeroy, S.L., Golub, T.R., Lander, E.S., and Mesirov, J.P. (2005). Gene set enrichment analysis: a knowledge-based approach for interpreting genome-wide expression profiles. Proc Natl Acad Sci U S A *102*, 15545-15550. 10.1073/pnas.0506580102.

Figure 1

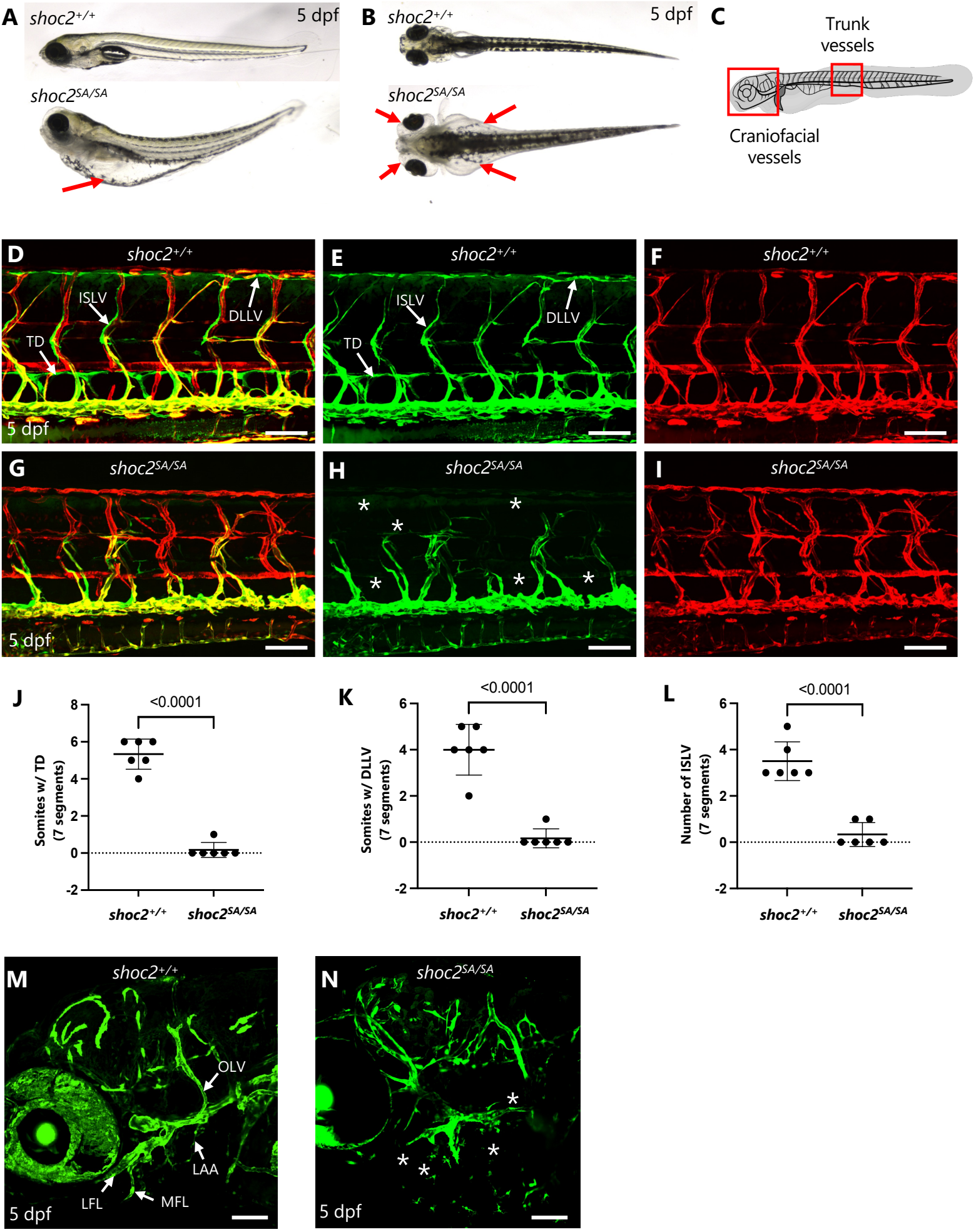
A
shoc2+/+
5 dpf
shoc2SA/SA
B
shoc2+/+
5 dpf
shoc2SA/SA
C
Trunk vessels
Craniofacial vessels
D
shoc2+/+
ISLV
DLLV
TD
5 dpf
E
shoc2+/+
ISLV
DLLV
TD
F
shoc2+/+
G
shoc2SA/SA
5 dpf
H
shoc2SA/SA
I
shoc2SA/SA
J
<0.0001
Somites w/ TD (7 segments)
shoc2+/+
shoc2SA/SA
K
<0.0001
Somites w/ DLLV (7 segments)
shoc2+/+
shoc2SA/SA
L
<0.0001
Number of ISLV (7 segments)
shoc2+/+
shoc2SA/SA
M
shoc2+/+
OLV
LAA
LFL
MFL
5 dpf
N
shoc2SA/SA
5 dpf

Figure 2

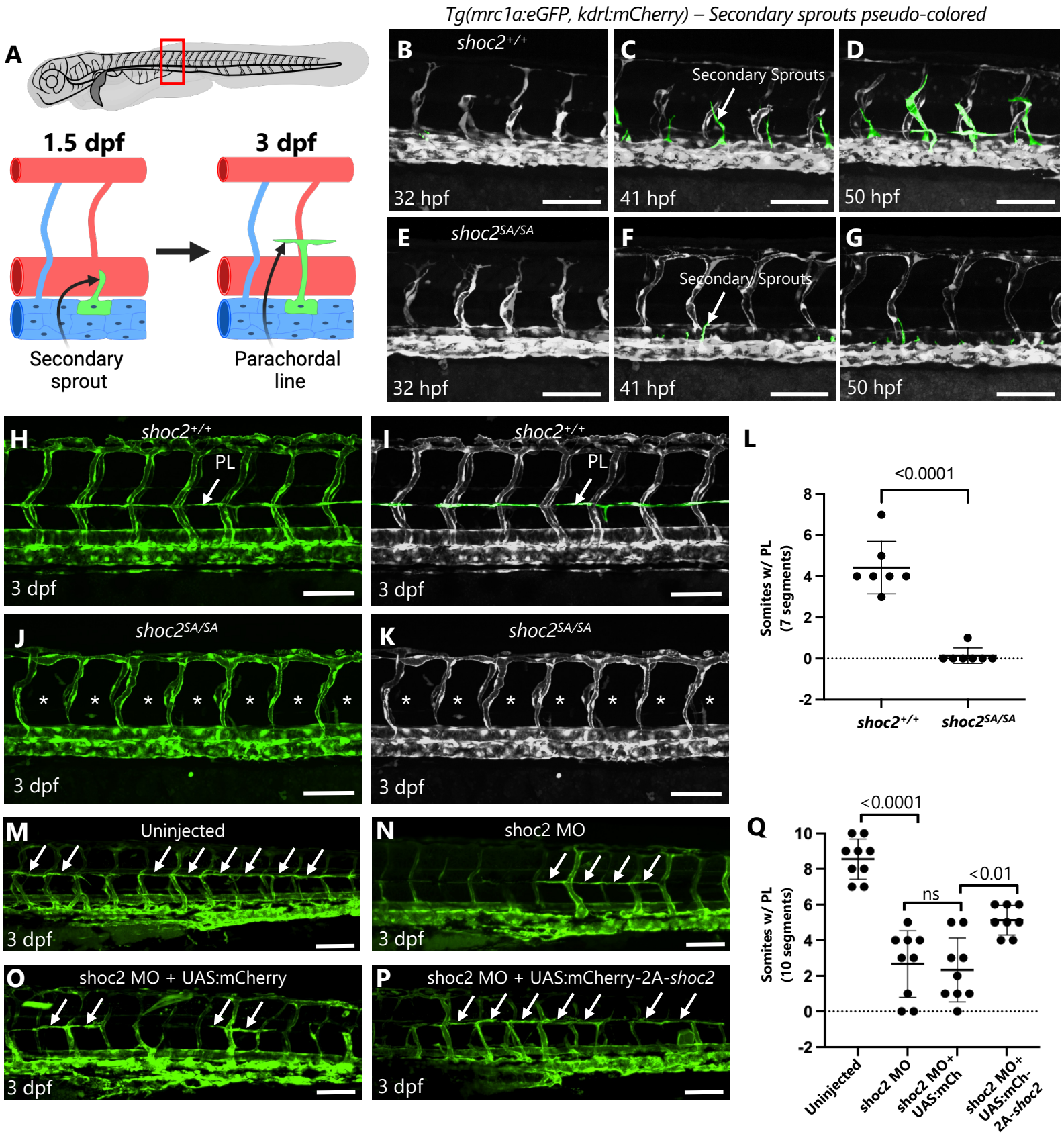
A
1.5 dpf
3 dpf
Secondary sprout
Parachordal line
Tg(mrc1a:eGFP, kdrl:mCherry) – Secondary sprouts pseudo-colored
B
shoc2+/+
32 hpf
C
Secondary Sprouts
41 hpf
D
50 hpf
E
shoc2SA/SA
32 hpf
F
Secondary Sprouts
41 hpf
G
50 hpf
H
shoc2+/+
PL
3 dpf
I
shoc2+/+
PL
3 dpf
J
shoc2SA/SA
3 dpf
K
shoc2SA/SA
3 dpf
L
<0.0001
Somites w/ PL (7 segments)
shoc2+/+
shoc2SA/SA
M
Uninjected
3 dpf
N
shoc2 MO
3 dpf
O
shoc2 MO + UAS:mCherry
3 dpf
P
shoc2 MO + UAS:mCherry-2A-shoc2
3 dpf
Q
<0.0001
ns
<0.01
Somites w/ PL (10 segments)
Uninjected
shoc2 MO
shoc2 MO+ UAS:mCh
shoc2 MO+ UAS:mCh-2A-shoc2

Figure 3

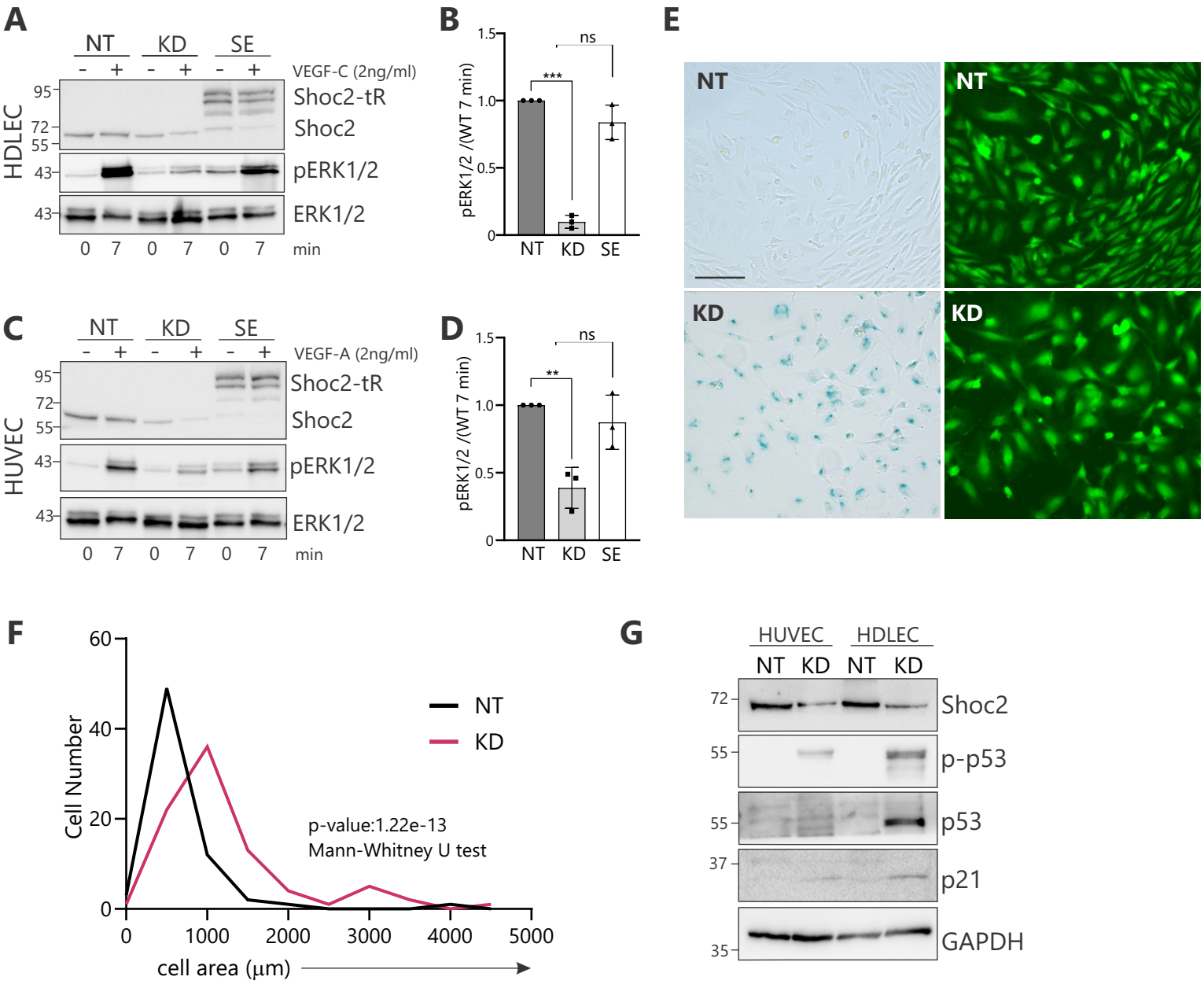
A
NT
KD
SE
- + - + - +
VEGF-C (2ng/ml)
HDLEC
95
72
55
43
43
Shoc2-tR
Shoc2
pERK1/2
ERK1/2
0 7 0 7 0 7
min
B
pERK1/2 /(WT 7 min)
1.5
1.0
0.5
0
ns
***
NT KD SE
C
NT
KD
SE
- + - + - +
VEGF-A (2ng/ml)
HUVEC
95
72
55
43
43
Shoc2-tR
Shoc2
pERK1/2
ERK1/2
0 7 0 7 0 7
min
D
pERK1/2 /(WT 7 min)
1.5
1.0
0.5
0
ns
**
NT KD SE
E
NT
NT
KD
KD
F
Cell Number
60
40
20
0
NT
KD
p-value:1.22e-13
Mann-Whitney U test
0 1000 2000 3000 4000 5000
cell area (μm)
G
HUVEC
HDLEC
NT KD NT KD
72
55
55
37
35
Shoc2
p-p53
p53
p21
GAPDH

Figure 4

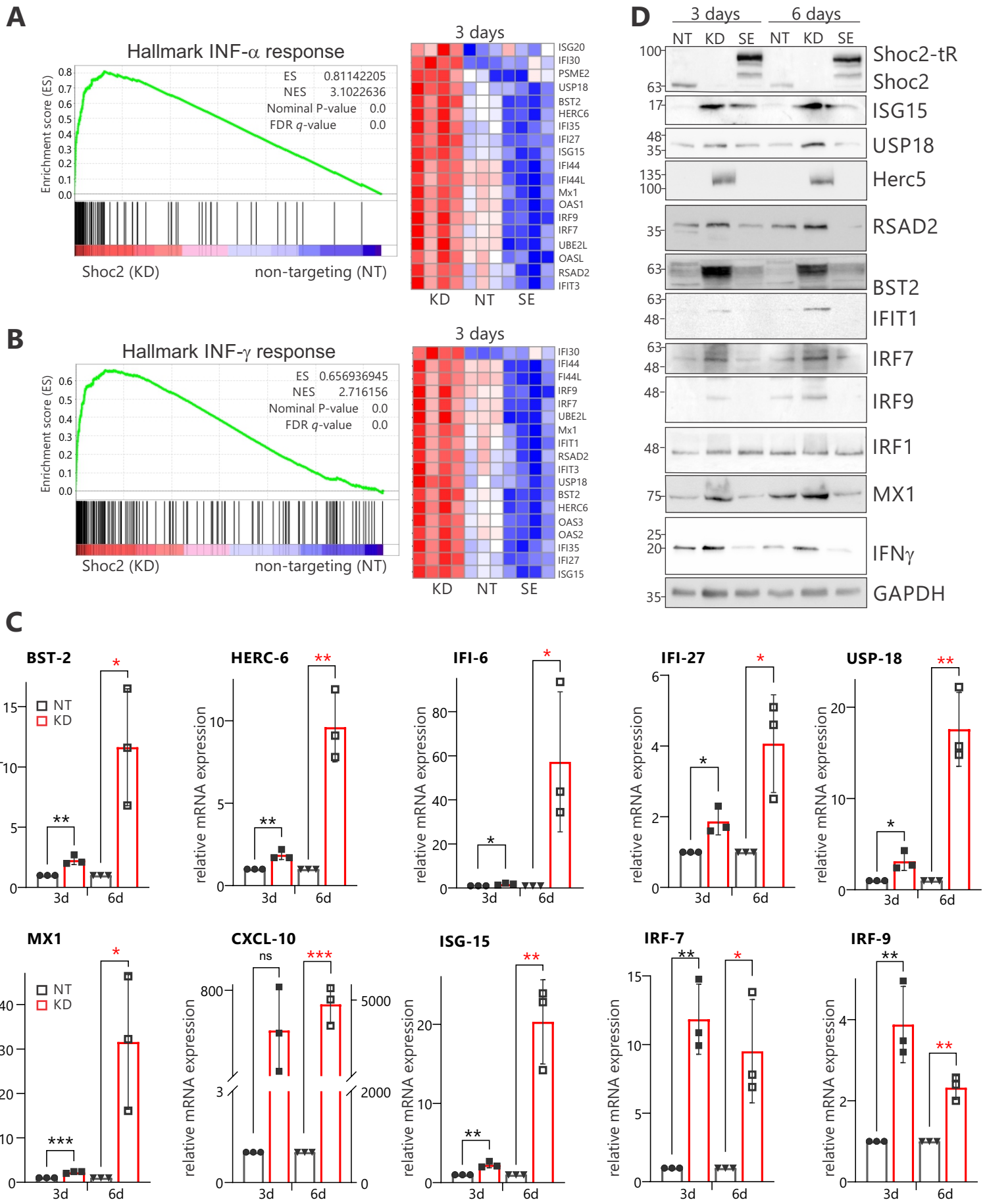
A
Hallmark INF-α response
Enrichment score (ES)
ES 0.81142205
NES 3.1022636
Nominal P-value 0.0
FDR q-value 0.0
Shoc2 (KD)
non-targeting (NT)
3 days
ISG20
IFI30
PSME2
USP18
BST2
HERC6
IFI35
IFI27
ISG15
IFI44
IFI44L
Mx1
OAS1
IRF9
IRF7
UBE2L
OASL
RSAD2
IFIT3
KD NT SE
B
Hallmark INF-γ response
ES 0.656936945
NES 2.716156
Nominal P-value 0.0
FDR q-value 0.0
3 days
IFI30
IFI44
FI44L
IRF9
IRF7
UBE2L
Mx1
IFIT1
RSAD2
IFIT3
USP18
BST2
HERC6
OAS3
OAS2
IFI35
IFI27
ISG15
D
3 days
6 days
NT KD SE NT KD SE
Shoc2-tR
Shoc2
ISG15
USP18
Herc5
RSAD2
BST2
IFIT1
IRF7
IRF9
IRF1
MX1
IFNγ
GAPDH
C
BST-2
HERC-6
IFI-6
IFI-27
USP-18
MX1
CXCL-10
ISG-15
IRF-7
IRF-9
relative mRNA expression
NT
KD
3d
6d
ns

Figure 5

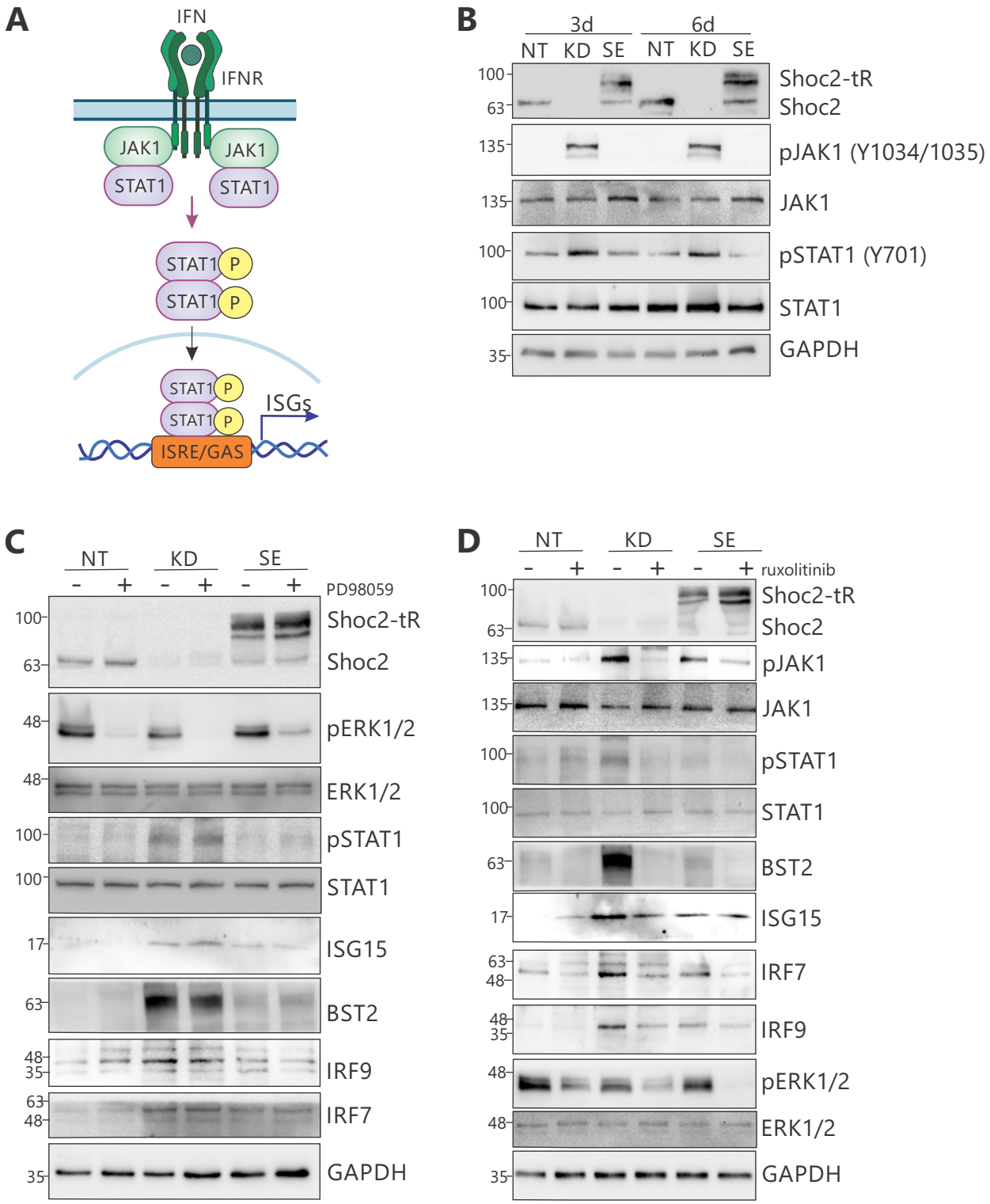
A
IFN
IFNR
JAK1
JAK1
STAT1
STAT1
STAT1
P
STAT1
P
STAT1
P
STAT1
P
ISGs
ISRE/GAS
B
3d
6d
NT
KD
SE
NT
KD
SE
100
63
Shoc2-tR
Shoc2
135
pJAK1 (Y1034/1035)
135
JAK1
100
pSTAT1 (Y701)
100
STAT1
35
GAPDH
C
NT
KD
SE
-
+
-
+
-
+
PD98059
100
63
Shoc2-tR
Shoc2
48
pERK1/2
48
ERK1/2
100
pSTAT1
100
STAT1
17
ISG15
63
BST2
48
35
IRF9
63
48
IRF7
35
GAPDH
D
NT
KD
SE
-
+
-
+
-
+
ruxolitinib
100
63
Shoc2-tR
Shoc2
135
pJAK1
135
JAK1
100
pSTAT1
100
STAT1
63
BST2
17
ISG15
63
48
IRF7
48
35
IRF9
48
pERK1/2
48
ERK1/2
35
GAPDH

Figure 6

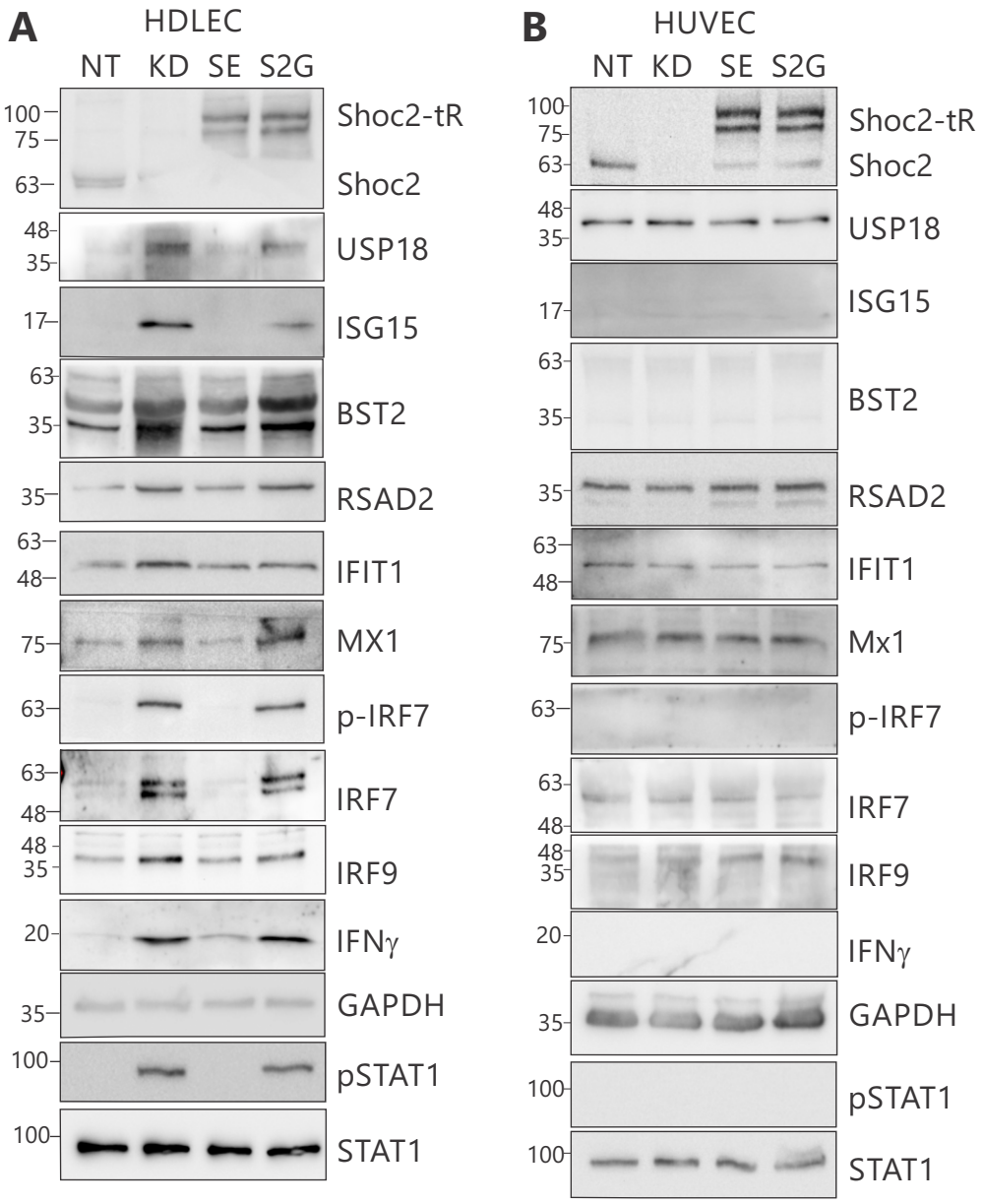
A
HDLEC
NT KD SE S2G
100
75
63
Shoc2-tR
Shoc2
48
35
USP18
17
ISG15
63
35
BST2
35
RSAD2
63
48
IFIT1
75
MX1
63
p-IRF7
63
48
IRF7
48
35
IRF9
20
IFNγ
35
GAPDH
100
pSTAT1
100
STAT1
B
HUVEC
NT KD SE S2G
100
75
63
Shoc2-tR
Shoc2
48
35
USP18
17
ISG15
63
35
BST2
35
RSAD2
63
48
IFIT1
75
Mx1
63
p-IRF7
63
48
IRF7
48
35
IRF9
20
IFNγ
35
GAPDH
100
pSTAT1
100
STAT1

Figure 7

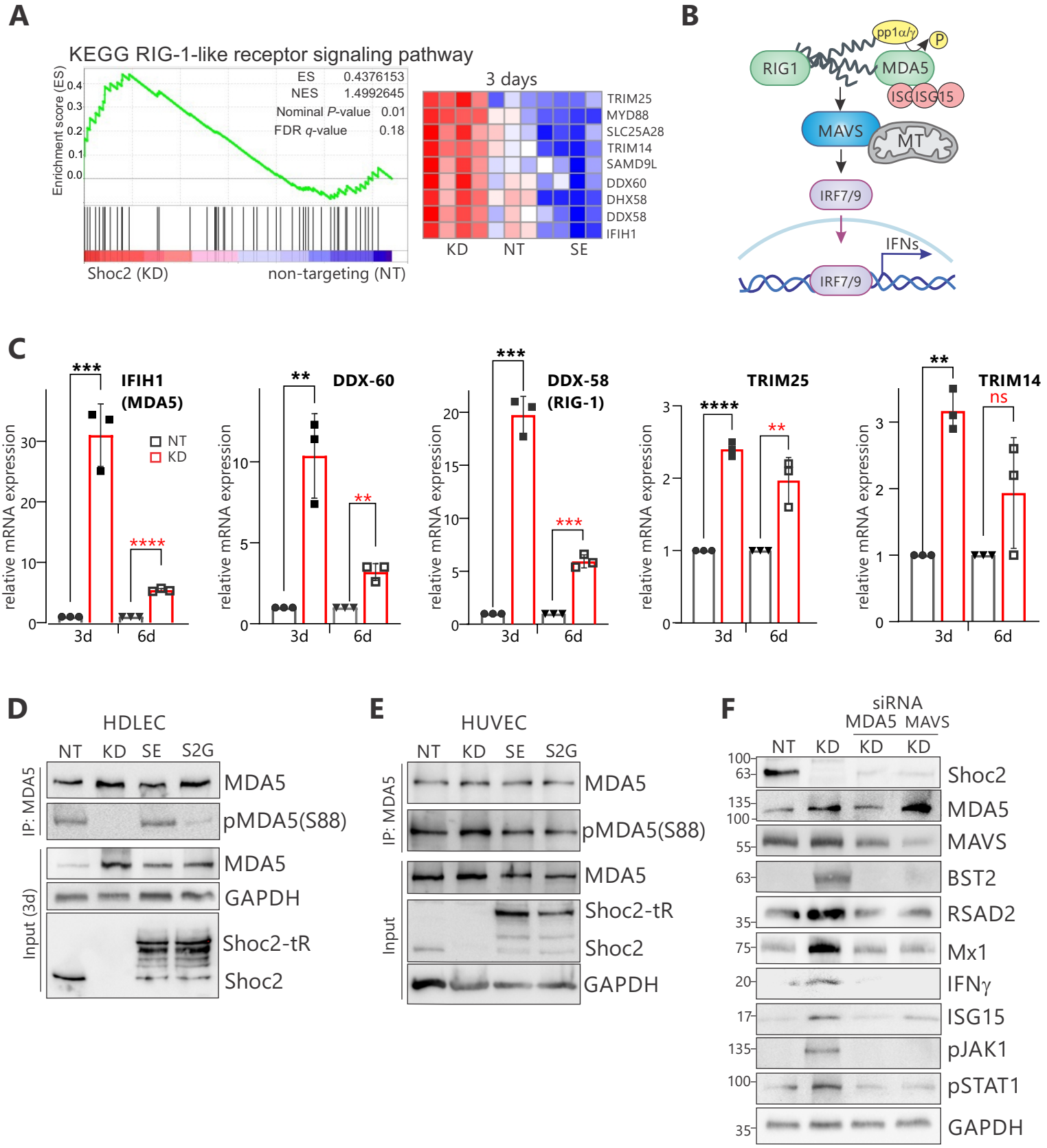
A
KEGG RIG-1-like receptor signaling pathway
Enrichment score (ES)
ES 0.4376153
NES 1.4992645
Nominal P-value 0.01
FDR q-value 0.18
Shoc2 (KD)
non-targeting (NT)
3 days
TRIM25
MYD88
SLC25A28
TRIM14
SAMD9L
DDX60
DHX58
DDX58
IFIH1
KD NT SE
B
pp1α/γ
P
RIG1
MDA5
ISG15
MAVS
MT
IRF7/9
IFNs
IRF7/9
C
IFIH1 (MDA5)
DDX-60
DDX-58 (RIG-1)
TRIM25
TRIM14
ns
NT
KD
relative mRNA expression
3d
6d
D
HDLEC
NT KD SE S2G
IP: MDA5
MDA5
pMDA5(S88)
Input (3d)
MDA5
GAPDH
Shoc2-tR
Shoc2
E
HUVEC
NT KD SE S2G
IP: MDA5
MDA5
pMDA5(S88)
Input
MDA5
Shoc2-tR
Shoc2
GAPDH
F
siRNA
MDA5 MAVS
NT KD KD KD
Shoc2
MDA5
MAVS
BST2
RSAD2
Mx1
IFNγ
ISG15
pJAK1
pSTAT1
GAPDH

Figure 8

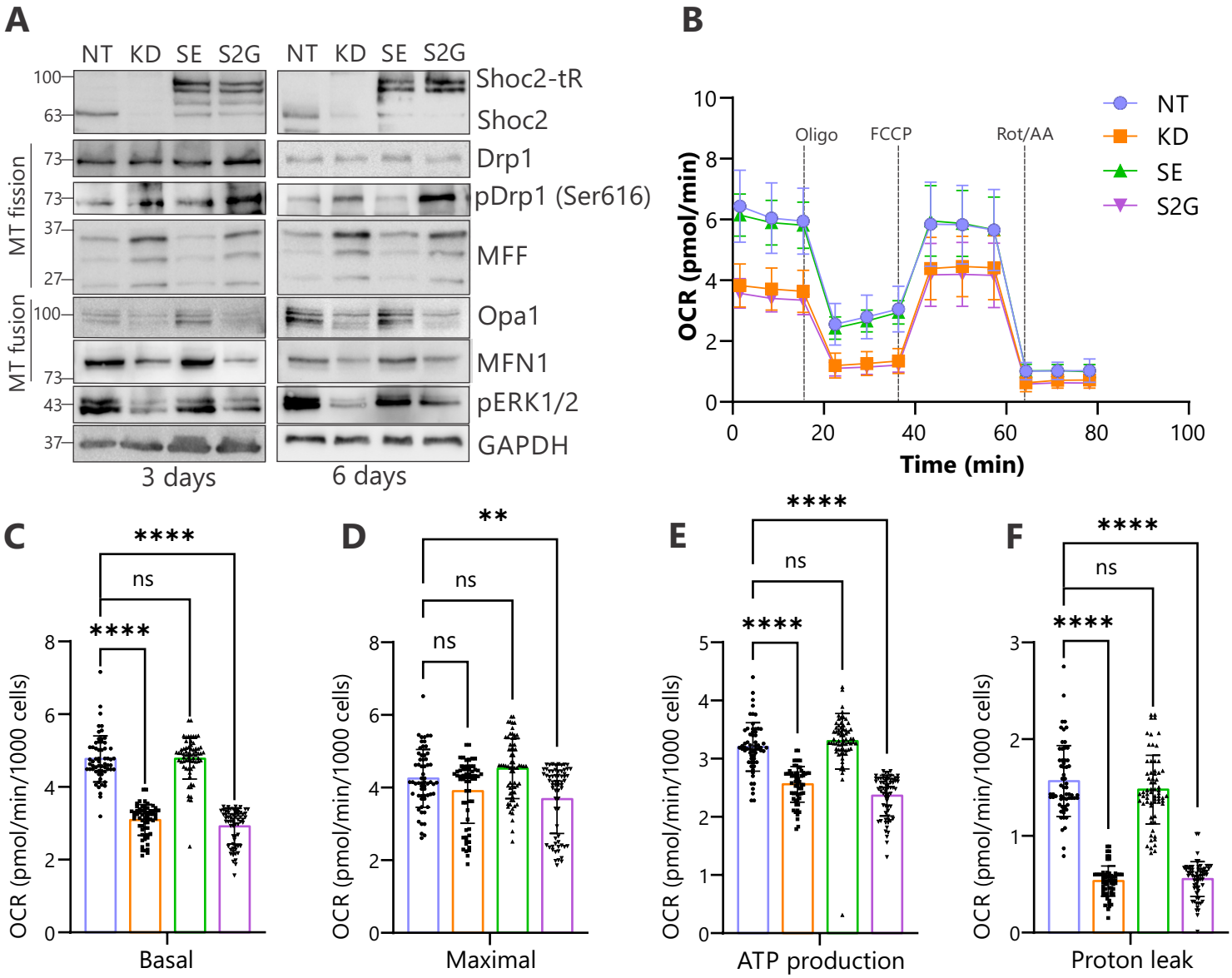
A
NT KD SE S2G NT KD SE S2G
Shoc2-tR
Shoc2
Drp1
pDrp1 (Ser616)
MFF
Opa1
MFN1
pERK1/2
GAPDH
MT fission
MT fusion
3 days
6 days
B
OCR (pmol/min)
Time (min)
Oligo
FCCP
Rot/AA
NT
KD
SE
S2G
C
D
E
F
OCR (pmol/min/1000 cells)
Basal
Maximal
ATP production
Proton leak
****
ns
**

Figure 9

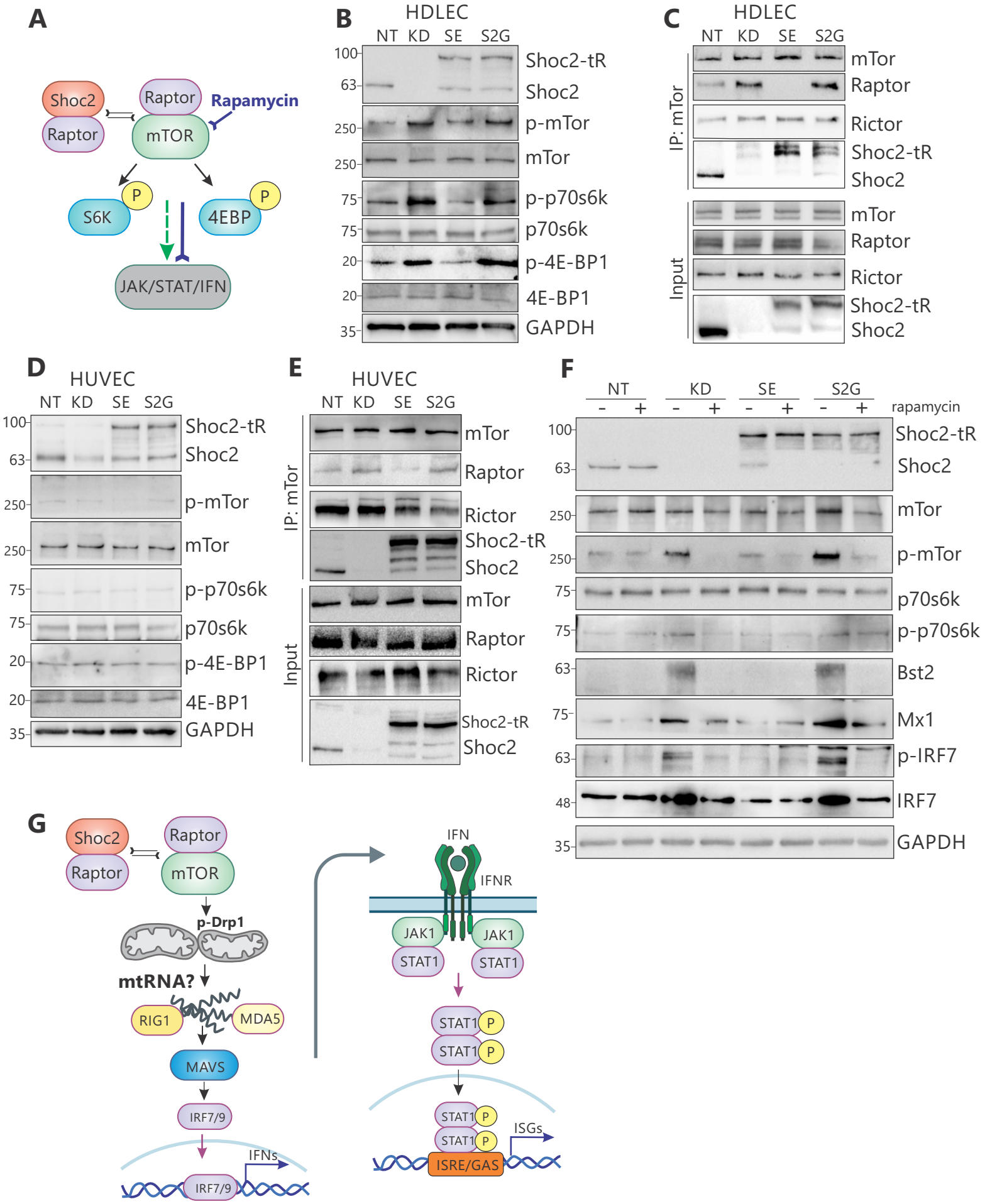
A
Shoc2
Raptor
Raptor
mTOR
Rapamycin
S6K
P
4EBP
P
JAK/STAT/IFN
B
HDLEC
NT KD SE S2G
100
63
250
250
75
75
20
20
35
Shoc2-tR
Shoc2
p-mTor
mTor
p-p70s6k
p70s6k
p-4E-BP1
4E-BP1
GAPDH
C
HDLEC
NT KD SE S2G
IP: mTor
mTor
Raptor
Rictor
Shoc2-tR
Shoc2
Input
mTor
Raptor
Rictor
Shoc2-tR
Shoc2
D
HUVEC
NT KD SE S2G
100
63
250
250
75
75
20
20
35
Shoc2-tR
Shoc2
p-mTor
mTor
p-p70s6k
p70s6k
p-4E-BP1
4E-BP1
GAPDH
E
HUVEC
NT KD SE S2G
IP: mTor
mTor
Raptor
Rictor
Shoc2-tR
Shoc2
Input
mTor
Raptor
Rictor
Shoc2-tR
Shoc2
F
NT KD SE S2G
- + - + - + - +
rapamycin
100
63
250
250
75
75
63
75
63
48
35
Shoc2-tR
Shoc2
mTor
p-mTor
p70s6k
p-p70s6k
Bst2
Mx1
p-IRF7
IRF7
GAPDH
G
Shoc2
Raptor
Raptor
mTOR
p-Drp1
mtRNA?
RIG1
MDA5
MAVS
IRF7/9
IFNs
IRF7/9
IFN
IFNR
JAK1
JAK1
STAT1
STAT1
STAT1
P
STAT1
P
STAT1
P
STAT1
P
ISGs
ISRE/GAS